nature plants

Article

https://doi.org/10.1038/s41477-026-02270-3

Membrane remodelling mediates lipopeptide-induced immunity in *Arabidopsis*

Received: 28 July 2025

Accepted: 10 March 2026

Published online: 20 April 2026

Check for updates

Guillaume Gilliard[1,2,22,28], Jelena Pršić[3,28], Jean-Marc Crowet[4], Catherine Chemotti[1], Jahed Ahmed[5], Joseph Lorent[6], Marie-Dominique Jolivet[7], Sabrina Egli[8], Stéphane Egée[9], Guillaume Bouyer[9], Gaëlle Race[3], Lennard van Buren[10], Anke Van Den Berghe[10], Anthony Argüelles-Arias[3], Marion Mathelié-Guinlet[11,23], Heba Ibrahim[10,24], Manon Genva[12], Laetitia Fouillen[5], Cécile Mirande-Bret[5], Oihana Razin[5], Brian Vue[5], Milan Zupunski[8], W. Patricio Luzuriaga-Loaiza[3], Estelle Deboever[1,25], M. Nail Nasir[1,26], Laurence Lins[1,27], Patrick Van Der Smissen[13], Farah Boubsi[3], Sabine Eschrig[14], Véronique Germain[5], Monica Höfte[15], Cyril Zipfel[16,17], Yves F. Dufrêne[10], Donatienne Tyteca[13], Alexandros Koutsioubas[18], Paola Brocca[19], Guido Grossman[8], Stefanie Ranf[2], Stephan Dorey[20], Barbara De Coninck[10], Thorsten Nürnberger[21], Sébastien Mongrand[5], Julien Gronnier[7], Valeria Rondelli[19], Magali Deleu[1,29] ✉ & Marc Ongena[3,29] ✉

Bacteria-derived lipopeptides are immunogenic triggers of host defences in metazoans and plants. Root-associated rhizobacteria produce cyclic lipopeptides that activate induced systemic resistance against microbial infection in various plant species. Whether and how these molecules are perceived at the plant cell surface remains elusive. Here we reveal that immune activation in *Arabidopsis thaliana* by the lipopeptide elicitor surfactin is mediated via a specific interaction with membrane sphingolipids. It relies on host membrane remodelling and subsequent activation of mechanosensitive ion channels. This mechanism leads to host defence potentiation and resistance to the necrotrophic fungus *Botrytis cinerea* and appears distinct from pattern-triggered immunity induced by classical host pattern recognition receptors. These results reveal a previously uncharacterized mechanism through which lipopeptides derived from non-pathogenic bacteria activate plant immune responses.

Lipopeptides (LPs) represent a prominent and structurally heterogeneous class of molecules in the broad spectrum of small, specialized metabolites synthesized by bacteria. Some LPs not only retain key functions for the ecological fitness of the producer (motility, biofilm formation, colonization, nutrient acquisition or antagonism towards competing neighbours)[1,2] but also act as triggers of immune responses that restrict pathogen infection of metazoans and plants[3,4]. Most LPs from plant-associated bacteria consist of a partially or fully cyclized oligopeptide linked to a single fatty acid chain. Some cyclic LPs (CLPs) from beneficial species of the genera *Pseudomonas* and *Bacillus* are potent elicitors of so-called induced systemic resistance (ISR) against microbial phytopathogens[4,5]. This CLP-induced resistance is a key process for biocontrol of crop diseases[6] and is phenotypically similar to the pathogen-induced systemic acquired resistance following pattern-triggered immunity (PTI) and/or effector-triggered immunity[7]. Like in animals, plant PTI relies on the detection of microbe-associated

A full list of affiliations appears at the end of the paper. ✉e-mail: magali.deleu@uliege.be; marc.ongena@uliege.be

molecular patterns (MAMPs) by plasma membrane (PM)-localized pattern-recognition receptors (PRRs)[8]. This leads to the phosphorylation of numerous substrate proteins and subsequent induction of prototypical cellular responses, such as apoplastic burst of reactive oxygen species ($[ROS]_{apo}$), cytosolic calcium ($[Ca^{2+}]_{cyt}$) burst, MAPK phosphorylation cascade and transcriptional reprogramming[9–13].

The ISR-triggering activity of CLPs has been amply demonstrated in many host species[4,5]. The relevance of these prominent bacterial secondary metabolites as elicitors of plant resistance is thus well established on the basis of macro-scale assessment of disease reduction. However, little progress has been made so far in the understanding of their mode of action. More specifically, the molecular mechanisms underlying CLP perception and immune activation in plant cells are still poorly understood in many aspects by contrast with PTI, which has been the focus of amazingly active research. In this work, we selected surfactin (Srf) (Fig. 1a), produced by plant-beneficial bacilli[1,14], as it represents one of the best-characterized bacterial compounds known to induce resistance in several plant species against a broad range of microbial pathogens[4]. Using Srf as a model, we investigated the mechanism of CLP interaction with *Arabidopsis* root cells and unveiled a non-canonical process underpinning immune stimulation by this ecologically potent microbial metabolite.

Induction of systemic defence responses

In *Arabidopsis thaliana* ecotype Col-0 (hereafter, *Arabidopsis*), root treatment with purified Srf (at 10 µM, previously determined as the minimal active concentration[15] and used as a mix of naturally produced homologues slightly differing in the length of the fatty acid tail; Extended Data Fig. 1a) triggers ISR and significantly reduces leaf infection by the grey mould pathogen *Botrytis cinerea* (Fig. 1b). The indole alkaloid camalexin is the major phytoalexin in *Arabidopsis* and plays a crucial role in pathogen resistance[16]. As this antimicrobial compound is toxic to *B. cinerea*[17,18], we hypothesized that it may accumulate upon Srf treatment and be involved in the systemic resistance observed. Accordingly, we measured significantly higher amounts of this phytoalexin in infected leaves of Srf-treated plants than in mock treatment (Fig. 1c). The key role of camalexin in disease control was confirmed by the loss of Srf-triggered resistance in the *pad3* mutant impaired in its synthesis[18,19] (Fig. 1d). In a similar set-up (see Fig. 1e for a schematic representation of the assay), plants pretreated with Srf at the root level also displayed a stronger $[ROS]_{apo}$ response in leaves upon perception of chito-oligosaccharide DP8 (CO8) used as a representative fungal pattern (Fig. 1f,g) or in response to flg22 as a bacterial MAMP (Extended Data Fig. 1b,c) than in leaves treated only with MAMPs. This systemic immune activation (SIA) response thus represents a solid and relevant proxy for Srf-induced priming of plant systemic defences.

A unique early immune response

We next investigated immune events induced by Srf at the cellular level in root tissues. We first performed quantitative and time-resolved measurements of early responses commonly associated with classical MAMP perception in *Arabidopsis* and other plants. A $[ROS]_{apo}$ burst is almost invariably associated with PTI[10], but in contrast to treatment with MAMPs, we did not observe such a response in Srf-treated *Arabidopsis* root cells using a chemiluminescence assay (Fig. 2a). Srf-mediated ISR against *B. cinerea* is also fully retained in the *rbohD* mutant lacking the PM NADPH oxidase RBOHD, which is responsible for MAMP-induced $[ROS]_{apo}$ burst[20,21] (Extended Data Fig. 1d). In contrast, we observed that Srf elicits a consistent increase in intracellular ROS ($[ROS]_{intra}$) using the biosensor HyPer7-cyto[22] (Fig. 2b,c) or the fluorescent probe dichloro-dihydro-fluorescein diacetate (DCFH-DA) (Extended Data Fig. 1e,f). This response is retained in the *rbohD* mutant (Extended Data Fig. 1g), suggesting that it is not caused by the uptake of apoplastic ROS via aquaporins (see Extended Data Fig. 1h for the response to flg22) but could originate from other organelles as reported for abiotic stresses or other small microbial compounds[10,23–25].

Ca^{2+} influx is typically associated with PTI in plants[11]. Luminescence measurement in whole roots of the Col-0^{AEQ} reporter line revealed no significant $[Ca^{2+}]_{cyt}$ increase following Srf elicitation, in contrast to the increase observed upon flg22 (Extended Data Fig. 2a) or chitin treatment (Extended Data Fig. 2b), suggesting a low and/or transient response to the CLP. R-GECO1 $[Ca^{2+}]_{cyt}$ sensor imaging[26,27] (Extended Data Fig. 2c,d), however, revealed a subtle but consistent Ca^{2+} response to Srf (Fig. 2d) that differs from the kinetics typically observed for responses to flg22 (Extended Data Fig. 2e). Via fluorescence stereomicroscopy, we also observed an Srf-induced Ca^{2+} response in the *UBQ10*::*GCaMP3* reporter line[28], allowing imaging with a larger field of view and visualization of Ca^{2+} signals in root zones more distal from the tip (Fig. 2e,f, Supplementary Video 1 and Extended Data Fig. 2f). Both high-resolution Ca^{2+} sensor assays support the potential of Srf to induce a consistent and specific Ca^{2+} response in root tissues.

We also observed that Srf treatment leads to medium alkalinization within minutes (Extended Data Fig. 2g), which is associated with H^+/K^+ exchange. Both Ca^{2+} and K^+ fluxes strongly modulate cell membrane potential[12], and accordingly, we observed a marked PM depolarization in root cells upon the addition of Srf, as revealed by internalization of the DiBAC4(3) fluorescent probe[29] (Fig. 2g,h). Interestingly, Srf induces similar early responses in protoplasts derived from root cells. We consistently observed a $[ROS]_{intra}$ burst (Extended Data Fig. 1i,j), a significant Ca^{2+} burst using Col-0^{AEQ} (Extended Data Fig. 2h,i) or upon loading with the Fluo4-AM probe (Extended Data Fig. 2j) and a clear PM depolarization (Extended Data Fig. 2k–m). We thus next used these wall-free cells for patch-clamp electrophysiology experiments and observed that Srf elicited a fast and transient response with a strong inward current increase (Fig. 2i,j) compatible with Ca^{2+} influx through ion channels. This provides direct evidence for Srf-mediated induction of ion fluxes across the PM. As no significant increase in conductivity was measured in the medium following Srf treatment (Extended Data Fig. 2n), the CLP does not affect PM integrity and does not cause massive electrolyte leakage. Viability tests also confirmed that Srf is not toxic to *Arabidopsis* root cells (Extended Data Fig. 2o) or protoplasts (Extended Data Fig. 2p) at the concentration used.

Next to these events occurring in the first minutes after elicitation, we wanted to explore changes in the root transcriptome profile possibly induced by Srf within hours. We performed time-course RNAseq analysis using the same set-up as previously reported for flg22 and chitin in a separate study[30] to confront our data for Srf with those obtained for these MAMPs. Our data revealed a limited transcriptional response to Srf elicitation across all sampling times, with a total of 246 differentially expressed genes ($\log_2$(fold change) > 1, $P < 0.05$; Extended Data Fig. 3a) compared with approximately 7,600 and 3,800 differentially expressed genes reported upon flg22 and chitin treatment, respectively[30,31]. Most of the Srf-altered genes are upregulated, and their number steadily increases over the first 6 h (Extended Data Fig. 3b)[30]. For some selected genes, differential expression in RNAseq was confirmed by quantitative PCR with reverse transcription (RT–qPCR) (Extended Data Fig. 3c). In contrast to treatment with classical MAMPs, which is associated with substantial transcriptional reprogramming[31], the expression of genes typically associated with early immune signalling or with defence mechanisms is not affected by Srf (Extended Data Fig. 3d). Srf immune stimulation thus does not massively alter defence gene expression, in contrast to PTI.

Sensing independent of typical PRR systems

Globally, our data show that the immune outputs induced by Srf differ from those observed in PTI, and we hypothesized that plant cells sense CLPs through a mechanism distinct from classical MAMP recognition. MAMP sensing in PTI is well described. Upon the assembly of higher-order receptor complexes involving conserved co-receptors,

https://doi.org/10.1038/s41477-026-02270-3

PRRs activate receptor-like cytoplasmic kinases such as BIK1 and its closest homologue, PBL1, described as key convergent immune signalling hubs. We wanted to test the possible involvement of these immune components in Srf perception. Srf-induced ISR was still observed in *Arabidopsis* mutants lacking PRRs or co-receptors/adapters involved in the recognition of either bacteria-derived proteinaceous immunogenic patterns or acyl-chain epitopes such as medium-chain 3-hydroxy fatty acids[32,33] or more generally required for leucine-rich-repeat- and LysM-containing PRRs[34–36] (Extended Data Fig. 4). Srf was similarly still immunogenic in the *bik1 pbl1* double mutant lacking receptor-like cytoplasmic kinases. Although we only tested a small subset of the multitude of PRRs potentially expressed in *Arabidopsis*[9] and although early cellular signalling may occur independently of BIK1/PBL1 (ref. 27), these data suggest that *Arabidopsis* does not sense Srf via classical PRRs. This is in accordance with previous data on tobacco, where Srf remained active on protease-treated cells and did not induce a refractory state upon repeated Srf treatment, unlike what is typically observed for PTI[37].

Docking to GluCer for perception

Due to their amphipathic nature, CLPs readily interact with biological membranes and cause pore formation and membrane disruption, which are responsible for their antimicrobial activities[38]. We therefore hypothesized that Srf perception by root cells may be primarily due to its interaction with the lipid phase of the PM. Besides phospholipids and sterols, the sphingolipid glucosylceramides (GluCer) and glycosyl inositol phosphorylceramides (GIPCs) are key components required for membrane integrity and functionality[39–41] and are mostly located in the outer leaflet making up more than 30 mol% of *Arabidopsis* PM lipids.

We first experimentally investigated Srf–membrane interactions via isothermal titration calorimetry (ITC). To that end, we generated biomimetic liposomes with typical plant PM lipids including commercially available GluCer, PLPC (1-palmitoyl-2-linoleoyl-sn-glycero-3-phosphocholine as phospholipid) and β-sitosterol (Sito, as main sterol). ITC revealed a significantly higher binding affinity of Srf to binary or ternary liposome systems containing GluCer than to those containing other lipids (Fig. 3a and Supplementary Fig. 1). The thermodynamic parameters (Extended Data Fig. 5a) indicate that the binding of Srf to liposomes is spontaneous (negative ΔG) for all tested membrane compositions and slightly thermodynamically more favourable in the presence of GluCer (more negative ΔG). The positive enthalpy change ($\Delta H > 0$) combined with a large positive entropy change ($\Delta S > 0$) suggests that the interaction is predominantly driven by hydrophobic forces. The less positive ΔH in GluCer-containing membranes suggests a larger contribution of electrostatic interactions, such as hydrogen bonds and van der Waals interactions, than in membranes without GluCer.

At higher structural resolution, molecular dynamics (MD) using both coarse-grained (CG) and all-atom (AT) simulations on the same

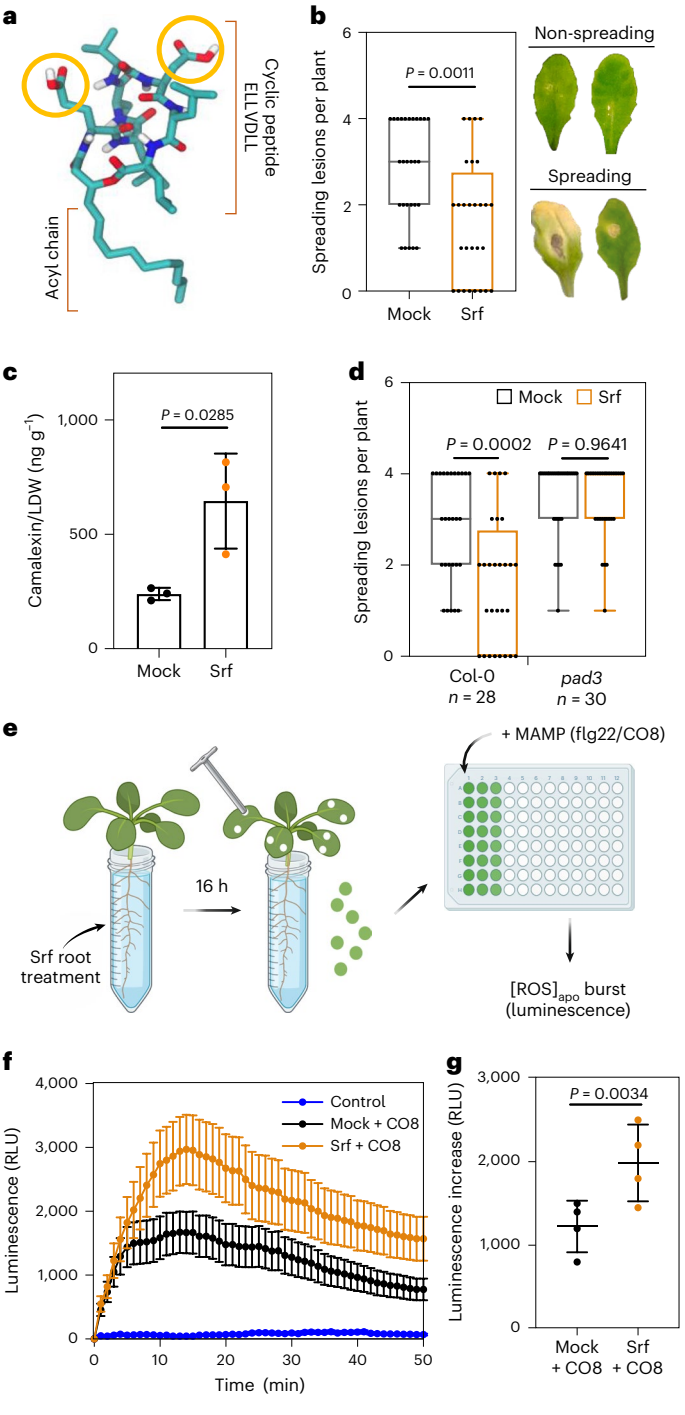

Fig. 1 | Srf triggers systemic resistance and defence responses in *Arabidopsis*. **a**, Structural model of Srf (C_{14} acyl chain) in water (Gromacs v.4.5.4). Red indicates O atoms, white indicates H, dark blue indicates N and light blue indicates C. Polar residues are circled in yellow; the non-polar part includes the remaining residues and the acyl chain. **b**, Disease incidence in *Arabidopsis* Col-0 pretreated at the root level with 10 µM Srf or mock (EtOH 0.1%) prior to *B. cinerea* infection on leaves. The data points indicate values obtained for individual plants in three independent experiments with total $n = 28$ for both treatments. The pictures show lesions typically observed on leaves of hydroponically grown *Arabidopsis* Col-0 plants 4 days post-infection. **c**, Camalexin accumulation in Col-0 leaves (in ng per g of leaf dry weight, LDW) at 96 hours post-infection with *B. cinerea*, after root treatment with Srf (10 µM) or mock (EtOH 0.1%). The data are shown as mean ± s.d. from one experiment, with each point corresponding to the value obtained for analysis of one single extract prepared from five independent plants pooled together. $n = 3$; the *P* value was obtained from a two-tailed *t*-test. **d**, Disease incidence in the *pad3* mutant compared to Col-0, both pretreated with Srf 10 µM or mock (EtOH 0.1%). The data points are as in **b** with total *n* indicated in the graph. **e**, SIA assay. **f**,**g**, $[ROS]_{apo}$ burst measured upon treatment with chitin (tested as CO8) on leaf discs prepared from Col-0 plants pretreated on roots with Srf (10 µM) or mock (DMSO 0.1%). 'Control' represents the leaf response to water treatment. **f** shows a typical trend for time-course measurement of CO8-induced $[ROS]_{apo}$ in one representative experiment. The data are shown as mean luminescence ± s.d. with $n = 12–14$ leaf discs. **g** shows the quantification of $[ROS]_{apo}$ burst ($L_{max,15\,min} - L_0$) recorded in four independent experiments. The data are shown as mean ± s.d. ($n = 4$); the *P* value is from a two-tailed *t*-test. Each data point is the mean value of 11 to 24 leaf discs obtained in one single experiment. In **b** and **d**, the box plots show the median (centre line) and quartiles; the whiskers indicate the range, with bars extending from the lowest to the highest values. The *P* values were obtained from a two-tailed *t*-test (**b**) or from two-way analysis of variance (ANOVA) with Sidak's post-test (**d**). Illustration in **e** created in BioRender; Ongena, M. https://biorender.com/q5y85ti (2026).

https://doi.org/10.1038/s41477-026-02270-3

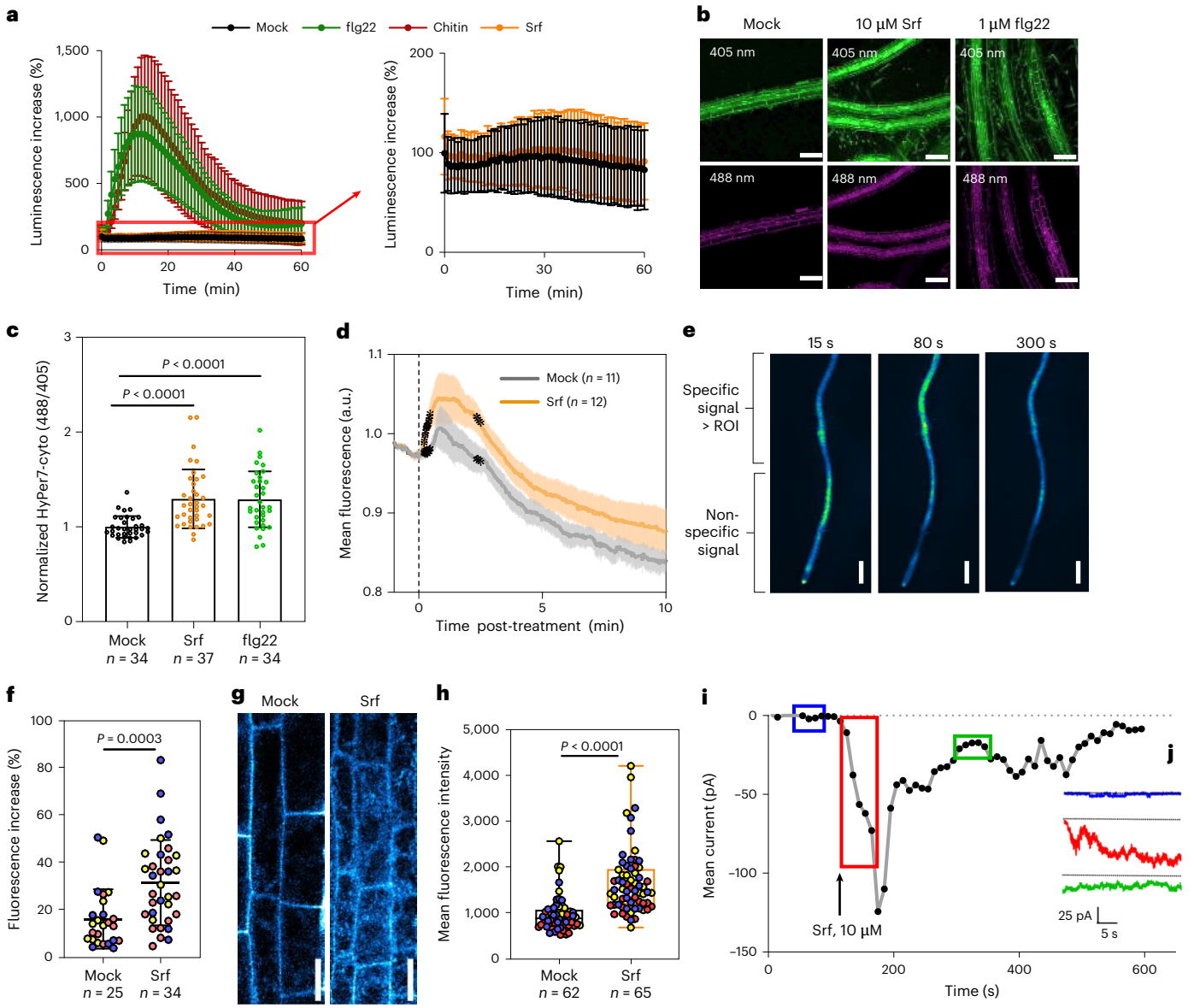

Fig. 2 | Srf induces atypical early immune responses in roots. a, Kinetics of $[ROS]_{apo}$ production in roots treated with 1 µM flg22, 100 µg ml^{-1} chitin or 10 µM Srf compared to mock (DMSO 0.1%). Relative luminescence is normalized to time 0. The data are shown as mean ± s.d. with $n = 18$; data are pooled from two independent experiments. **b**,**c**, $[ROS]_{intra}$ accumulation measured by HyPer7 fluorescence imaging of *Arabidopsis* Col-0 roots 25–30 min after treatment with 10 µM Srf, 1 µM flg22 or EtOH 0.1% (mock). **b** shows representative confocal images (top, excitation 405 nm, green, reduced form of sensor; bottom, 488 nm, magenta, oxidized sensor). Scale bars, 100 µm. **c** shows the quantification of ratiometric HyPer7 fluorescence (488/405 nm) upon the different treatments. The data are shown as mean ± s.d.; total *n* regions of interest (ROIs) are shown below each treatment from nine roots. The *P* values are from one-way ANOVA and Sidak's post-test. **d**, $[Ca^{2+}]_{cyt}$ sensing by R-GECO signal measurement (mean fluorescence intensity ± s.d.) in root tips treated with mock (DMSO 0.1%) or Srf (10 µM); the dashed vertical line indicates the treatment time. Statistically significant deviations are visualized through black asterisks on the curves at $P < 0.05$ (two-tailed *t*-test). **e**,**f**, Calcium response in roots of the *Arabidopsis UBQ10*::*GCaMP3* reporter line upon Srf treatment. **e** shows representative pseudo-coloured images of time-course changes in $[Ca^{2+}]_{cyt}$ fluorescence signal after elicitation with 10 µM Srf at the root tip. Scale bars, 2 mm. **f** shows the quantification of the $[Ca^{2+}]_{cyt}$ signal based on fluorescence increase $((F_{max} - F_0)/F_0)$ in the ROI after Srf (10 µM) or mock (DMSO 0.1%) treatment. Means ± s.d. were calculated from data in three independent experiments (individual measurements are shown in different colours) with the total *n* indicated. The *P* value is from a two-tailed Welch's *t*-test. **g**,**h**, PM depolarization in *Arabidopsis* Col-0 root epidermal cells. **g** shows confocal images of root cells stained with 6.25 µM DiBAC4(3) after treatment with Srf (10 µM) or mock (EtOH 0.1%). Scale bars, 20 µm. **h** shows box plots of scattered data points showing individual measurements (coloured on the basis of three independent experiments) of intracellular DiBAC4(3) fluorescence intensity of root cells treated with 10 µM Srf or the corresponding mock (EtOH 0.1%). The box plots show the median and quartiles; the whiskers indicate the range. The total numbers of ROIs used are indicated. The *P* value is from a two-tailed Mann–Whitney test. **i**,**j**, Representative recordings obtained in four experiments for membrane currents measured with a patch-clamp in Col-0 protoplasts during Srf (10 µM) perfusion. **i** shows the continuous mean membrane current across membrane patches calculated over a 10-s time frame, with Srf perfusion at 120 s. **j** shows representative single-channel recordings obtained in four independent experiments. The blue trace corresponds to the recording frame highlighted in blue in **i** (30 s before Srf addition), showing one channel opening. The red trace (red frame in **i**) represents the 30 s recording immediately after Srf addition, while the green trace (green frame in **i**) corresponds to the recovery phase, illustrating the transient nature of Srf-induced activation. The dotted line represents the zero current.

ternary lipid system showed a specific location of Srf in the vicinity of GluCer molecules (Fig. 3b,c). The radial distribution function showed a markedly higher probability of finding GluCer within 1.5 nm of the Srf molecules (Fig. 3d and Supplementary Fig. 2) compared with PLPC or Sito. Accordingly, the computation of the enrichment parameter (calculated as in ref. 42) revealed an 8.5 ± 1.1% increase in GluCer in the vicinity of Srf. In the AT simulations, hydrogen bonding frequency was also higher between Srf and the glucose of GluCer compared with PLPC or Sito (Fig. 3e,f), in accordance with the less positive ΔH of ITC (Extended Data Fig. 5a). These findings indicate that the preferential interaction arises from the specific chemical features of GluCer, and particularly its glucose moiety.

In a reverse genetics approach, we next tested Srf elicitor activity in vivo on the *Arabidopsis* ceramide synthase mutant *loh1* (LONGEVITY ASSURANCE 1 HOMOLOG1), which is depleted in complex sphingolipids[43,44]. We observed a strong reduction in local $[ROS]_{intra}$ response using *loh1xHyPer7-cyto* (Fig. 3g) or the DCFH-DA probe (Extended Data Fig. 5b) as well as impaired SIA in response to CO8 (Fig. 3i) and reduced systemic resistance to *B. cinerea* infection (Fig. 3k) compared with wild-type plants. We also tested the *moca1* (monocation-induced $[Ca^{2+}]_i$ increases 1) mutant, which is deficient in the first glycosylation of IPCs to generate GIPCs. Semi-quantitative sphingolipidomics showed that GIPCs are strongly decreased in *moca1* compared with the wild type and replaced by IPCs, whereas the GluCer level is not affected (Extended Data Fig. 5c), making this mutant an excellent tool to tackle the differential role of GluCer and GIPC in the context of Srf interaction with the PM. We observed that the ROS response observed via HyPer7 fluorescence imaging was still triggered by Srf in *moca1* (Fig. 3h), and this mutant conserved the SIA potential (Fig. 3j). Altogether, these observations show that Srf perception is predominantly mediated by GluCer, while GIPCs have a marginal role in this process. Such lipid-dependent $[ROS]_{intra}$ elicitation was also observed for other ISR-eliciting CLPs from beneficial pseudomonads, such as orfamide and WLIP[4], which resemble Srf in size and amphiphilic character (Extended Data Fig. 5d,e). The CLP immunogenic activity thus relies on an intricate interaction with PM sphingolipids, as reported for other microbial compounds[44–46].

PM remodelling and lipid reordering

By inserting into lipid bilayers, Srf may transiently affect the local structure of membranes. Indeed, neutron reflectivity (NR) experiments (see Supplementary Fig. 3 for deuterated Srf synthesis and characterization) demonstrated that Srf inserts exclusively and deeply into the outer leaflet of PLPC–Sito–GluCer model membranes (Fig. 4a). This is supported by MD simulation showing that the Srf peptide backbone preferentially positions at the level of the polar lipid heads of the membrane (Fig. 3c). Scattering length density (SLD) profiles from small-angle X-ray scattering (SAXS) on ternary liposomes (Fig. 4b,c), analysis of the nanoscale morphology of supported ternary bilayers by atomic force microscopy (AFM) (Extended Data Fig. 6a) and MD simulations (Extended Data Fig. 6b) showed membrane thinning caused by Srf insertion. SLD profiles obtained from NR on ternary supported bilayers confirm membrane thinning (from 40 to 36 Å) and indicate that thinning is more pronounced in ternary membranes than in membranes lacking GluCer (from 43 to 41 Å) (Extended Data Table 1). Membrane thinning is in accordance with the disordering effect of Srf on the lipid acyl chains as revealed by MD and suggested by wide-angle X-ray scattering (WAXS) (Extended Data Fig. 6c–e). Additionally, the presence of Srf resulted in a decrease of the hydrodynamic radius of ternary liposomes evidenced by dynamic light scattering (DLS) (Extended Data Fig. 6f,g) and in a smoother SAXS scattering profile for the ternary bilayer around the transferred **q**-vector values of 0.1 $Å^{-1}$ (Fig. 4b). These findings suggest a lateral redistribution of membrane components as observed in MD (Fig. 3b) and with Förster resonance energy transfer (FRET) assay on large unilamellar vesicles (LUVs) (Extended Data Fig. 6h). Altogether, these biophysical data highlight a remodelling of biomimetic membranes by Srf insertion, and we thus hypothesized that Srf would also affect the structure of native PM. Laurdan generalized polarization (GP) measurements first revealed that Srf treatment in root protoplasts significantly increases GP values, indicating a global stiffening of the membrane (Fig. 4d), a result also observed with PM-mimicking liposomes (Extended Data Fig. 6i). Complementary imaging using FlipperTR[47] in root protoplasts (Fig. 4e,f) and N^+-BODIPY[48] in native root epidermal cells (Fig. 4g,h) revealed that Srf enhances membrane lateral tension, consistent with an overall PM stiffening. As expected, this overall PM stiffening is less pronounced in the *loh1* mutant (Fig. 4i), supporting the key role of GluCer and providing a mechanistic link between GluCer deficiency in *loh1* and the associated biological responses to Srf.

At the molecular level, GluCer typically forms small clusters of two to seven molecules rather than large domains (Extended Data Fig. 7a–c and Supplementary Fig. 4). MD simulations show that Srf bridges GluCer molecules through hydrogen bonds (Fig. 3e,f). Srf inserts into membranes via the intermediate of its acyl chain through membrane packing defects (Extended Data Fig. 7d). Srf then plugs those defects at the bilayer surface (Extended Data Fig. 7e). This results in reduced lipid lateral mobility (Extended Data Fig. 7f) in support of the experimentally observed increase in membrane surface rigidity in giant unilamellar vesicles (GUVs) (Fig. 4j,k).

It is worth noting that Srf exerts opposite effects across membrane regions. In the polar headgroup region, it enhances rigidity (Fig. 4j,k and Extended Data Fig. 7f) through preferential interaction with the GluCer headgroup via hydrogen bonds (Fig. 3e,f), while it

Fig. 3 | Affinity for sphingolipids determines CLP-triggered immunity. **a**, Binding coefficient (K) of Srf to liposomes with different lipid compositions. Data from two independent experiments are represented. **b**, CG simulations of Srf in a PLPC–Sito–GluCer bilayer. Top views before (left) and after (right) Srf insertion are shown. PLPC is depicted in blue, Sito in green, GluCer in red and Srf in grey. **c**, Localization of Srf molecules in a PLPC–Sito–GluCer bilayer membrane after 500 ns of AT simulation. Srf is shown as thick sticks with O atoms in red, N atoms in dark blue and C atoms in light blue; GluCer is shown in green; and PLPC and Sito are shown in grey. **d**, Radial distribution functions of the different lipids towards Srf in the external leaflet of the ternary bilayer (that is, probability ($g(r)$) of finding the representative bead of the polar head of a defined lipid species at a certain distance (r) of Srf along the trajectory) obtained via CG simulation. Mean ± s.d. from one representative simulation out of four with similar results (see Supplementary Fig. 2 for replicates) is shown. **e**, Percentage of the AT simulation time for which hydrogen bonds were observed between the lipids or lipid chemical groups and one Srf molecule. PO4, phosphate from PLPC; Gly, glycerol of PLPC; Glu, glucose from GluCer; Cer, ceramide from GluCer; Sito, β-sitosterol. The data are shown as mean ± s.d.; $n = 6$ simulations. The letters indicate significantly different groups ($P < 0.05$, one-way ANOVA with Games–Howell's comparison post-test). **f**, Bridging effect of Srf on GluCer molecules inferred from MD. A top view from AT simulations (after 402 ns) shows hydrogen bonds (green) between Srf and GluCer in a PLPC–Sito–GluCer bilayer. GluCer glucose moieties are shown as sticks and Srf as wider sticks. **g**,**h**, $[ROS]_{intra}$ accumulation measured by ratiometric HyPer7-cyto fluorescence (488/405 nm) in roots of *loh1xHyPer7-cyto* (**g**) or *moca1xHyPer7-cyto* (**h**) reporter lines upon treatment with Srf (10 µM) compared to mock (EtOH 0.1%). The bars indicate mean ± s.d.; the data are from at least three independent biological replicates. Total ROIs (n) are indicated. The P values are from one-way ANOVA with Sidak's post-test. **i**,**j**, Quantification of $[ROS]_{apo}$ burst ($L_{max,15\,min} - L_0$) induced by CO8 in leaves of lipid mutant plants *loh1* (**i**) and *moca1* (**j**) pretreated on roots with Srf (10 µM) or mock (DMSO 0.1%) in three independent SIA experiments ($n = 3$). Each data point is the mean value obtained from six to nine leaf discs in one single experiment. The data are shown as mean ± s.d. The P values are from two-tailed t-tests. **k**, *B. cinerea* disease incidence in Col-0 and *loh1* mutants pretreated with Srf (10 µM) or mock (EtOH 0.1%). The data are from two independent experiments with total n indicated. The box plots show the median and quartiles; the whiskers indicate the range. The P values are from two-way ANOVA with Sidak's post-test.

https://doi.org/10.1038/s41477-026-02270-3

induces disorder within the lipid core (Extended Data Fig. 6c,d). This contrasting effect can be explained by a volumetric imbalance and a hydrophobic mismatch inside the membrane induced by Srf due to its peptide cycle being three times bigger than its acyl chain[49]. This increases the free space in the hydrophobic core region and induces a reduction in bilayer thickness.

Our data also display a clear Srf concentration-dependent effect on GP values (Fig. 4j), which indicates that a minimal number of Srf molecules must dock into the membrane platform to markedly modulate its structure. This explains why the activation of early responses by Srf requires threshold concentrations of 5–10 µM for both Ca^{2+} (Extended Data Fig. 8a) and $[ROS]_{intra}$ burst (Extended Data Fig. 8b), as revealed by additional assays on protoplasts. Such concentrations are substantially higher than those described for classical MAMPs, which usually trigger defence responses at low nanomolar doses, but they are similar to concentrations of microbial toxins required to interfere with host membrane integrity[44].

Immune activation involves mechanosensitive channels

Altogether, our data link Srf-induced PM remodelling with ion fluxes and early immune responses. We therefore hypothesized that physical constraints and increased lateral tension resulting from CLP insertion are sufficient to activate mechanosensitive ion channels, in a process

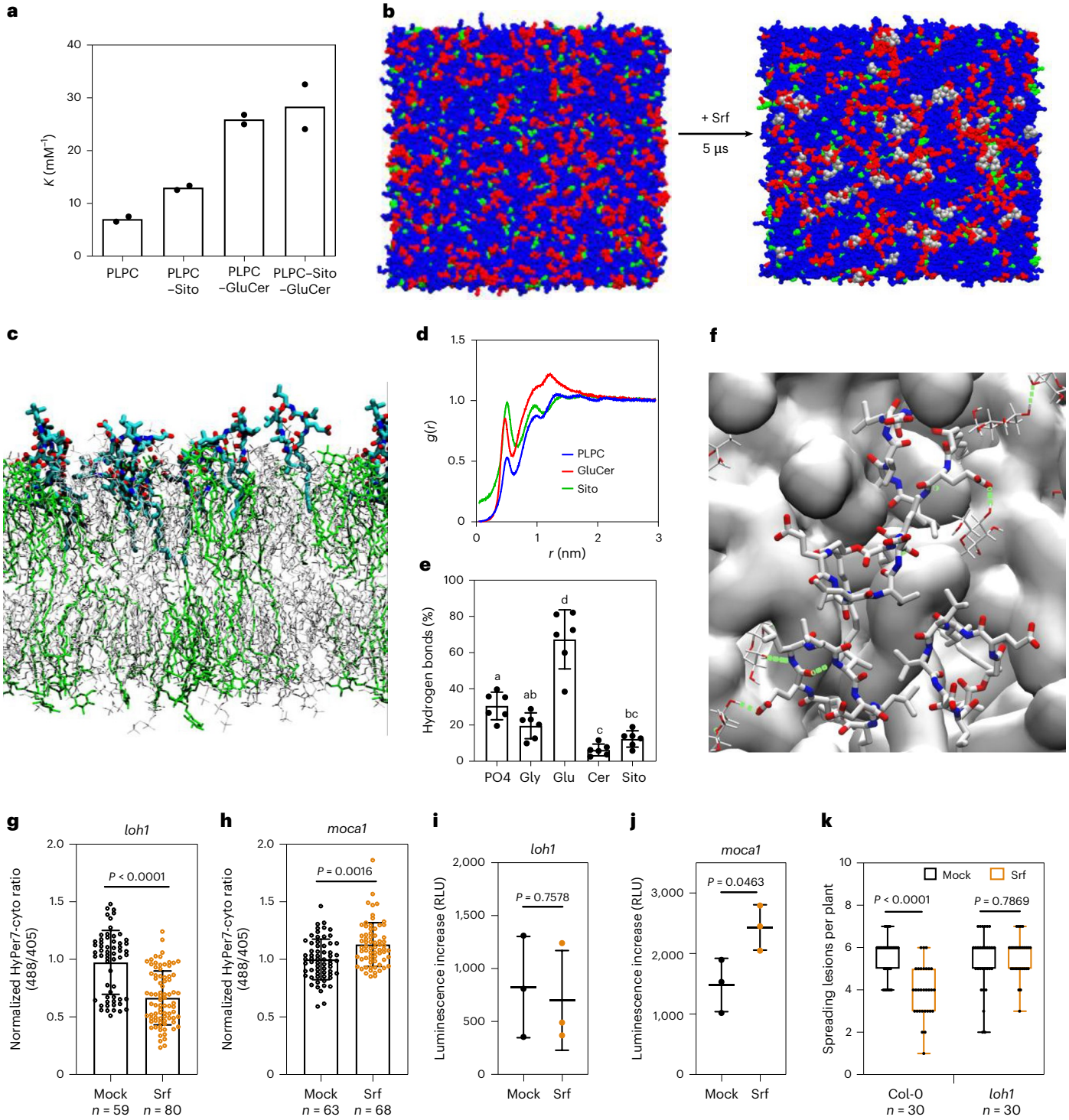

https://doi.org/10.1038/s41477-026-02270-3

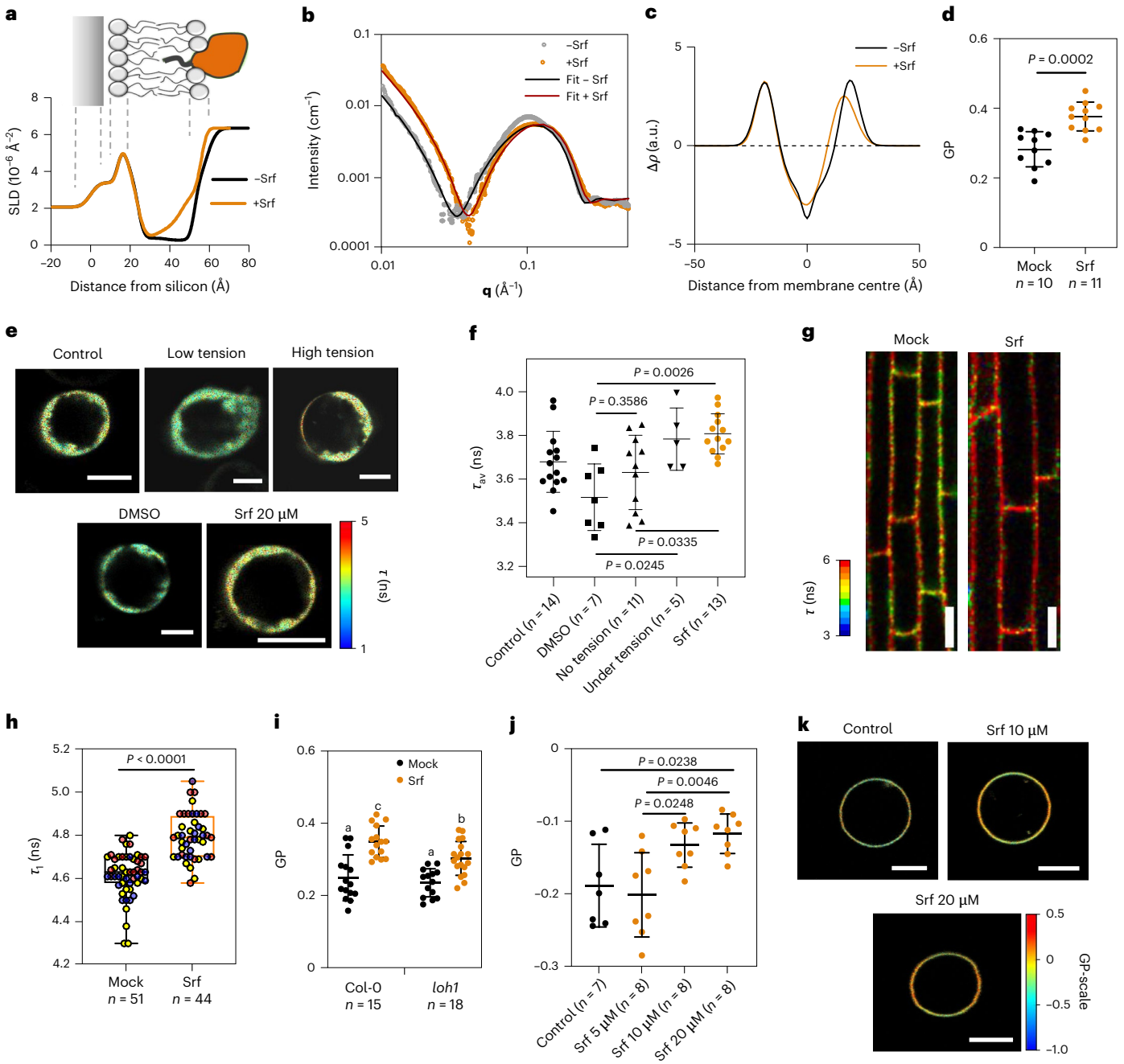

Fig. 4 | Srf causes PM remodelling. a, SLD profiles of supported PLPC–Sito–GluCer membranes before and after Srf addition (95:5 membrane:Srf molar ratio; 0.24 µM). A schematic linking SLD profiles and specific zones in the membrane is shown at the top. **b**, SAXS intensity profile of PLPC–Sito–GluCer LUVs before and after Srf incubation (95:5 molar ratio). **c**, SLD profiles obtained from SAXS. **d**, Global membrane rigidity measured by Laurdan GP upon the addition of Srf (10 µM) or not, in protoplasts from Col-0 roots. The data are shown as mean ± s.d.; *n* is indicated for each treatment, and the *P* value was obtained from a two-tailed *t*-test. **e**,**f**, Membrane tension sensing in protoplasts in isosmotic buffer (control) or treated with Srf, DMSO 0.1% or osmotic controls (hyperosmotic for low tension and hyposmotic for high tension) via fluorescence lifetime imaging (FLIM) of Flipper-TR-stained protoplasts. With this probe, some intracellular membranes can also be stained, but Srf is not expected to cross the PM, and it is thus assumed that the increase in Flipper-TR lifetime primarily reflects higher PM tension. **e** shows confocal images of protoplasts. Scale bars, 10 µm. **f** shows average Flipper-TR lifetimes (mean ± s.d.) in protoplasts (one symbol indicates one cell; *n* is indicated). The *P* values were derived from one-way ANOVA with Tukey's post-test. **g**,**h**, Membrane tension sensing in *Arabidopsis* root epidermal cells treated with Srf (10 µM) or mock (EtOH 0.1%) via FLIM of N^+-BODIPY-stained roots. **g** shows confocal images. Scale bars, 20 µm. **h** shows lifetime (τ_1) quantification of N^+-BODIPY at the PM in root cells; *n* roots were used as indicated coming from three independent experiments (one to three cells per root examined). The box plots show the median and quartiles; the whiskers indicate the range. The *P* value is from a two-tailed Mann–Whitney test. **i**, Global membrane rigidity via Laurdan GP measurements in Col-0 and *loh1* root protoplasts treated with mock (DMSO 0.1%) or Srf (10 µM). Mean ± s.d. of *n* replicates is shown, coming from eight and six experiments, respectively. The letters indicate significantly different groups ($P < 0.05$, two-way ANOVA with Tukey's post-test). **j**,**k**, Membrane surface rigidity measured by GP imaging of C-Laurdan-labelled GUVs exposed to increasing Srf concentrations. **j** shows the average C-Laurdan GP (mean ± s.d.) per GUV (one symbol indicates one GUV); the total *n* per treatment is indicated. The *P* values are from one-way ANOVA with Tukey's post-test. **k** shows associated confocal images. Scale bars, 5 µm.

https://doi.org/10.1038/s41477-026-02270-3

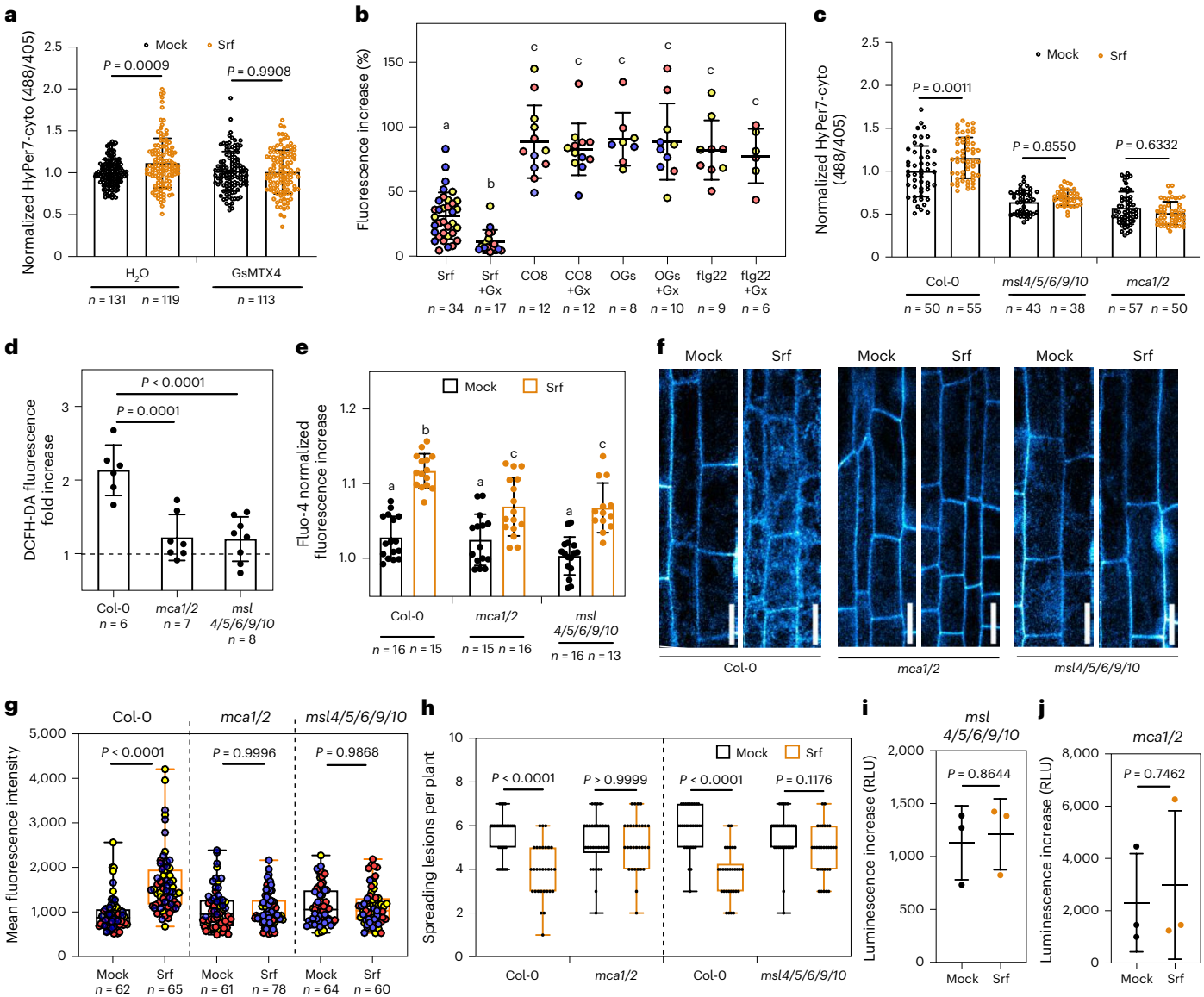

Fig. 5 | Srf activates mechanosensitive-channel-dependent immune responses. a, Accumulation of $[ROS]_{intra}$ measured by ratiometric HyPer7 fluorescence in *Arabidopsis* Col-0 root cells treated or not with the mechanosensitive channel inhibitor GsMTX4 prior to Srf (10 µM) or mock (DMSO 0.1%) exposure. **b**, $[Ca^{2+}]_{cyt}$ responses in roots of the *UBQ10*::*GCaMP3* reporter line pretreated or not with GsMTX4 (+Gx) before elicitation by Srf (10 µM), CO8 (150 µg ml^{-1}), oligogalacturonides $DP_{10–15}$ (OGs) (100 µg ml^{-1}) or flg22 (1 µM). The data are shown as mean ± s.d. from three experiments with total *n* indicated. The letters indicate significantly different groups at $P < 0.05$ (Brown–Forsythe ANOVA, Games–Howell's post-test). **c**, Accumulation of $[ROS]_{intra}$ measured via HyPer7 ratiometric signal in mock-treated (DMSO 0.1%) or Srf-treated (10 µM) roots of Col-0, *msl4/5/6/9/10* and *mca1/2* genotypes. **d**, $[ROS]_{intra}$ accumulation based on DCFH-DA fluorescence fold increase 30 min after Srf (10 µM) treatment (versus water as mock) in Col-0. *n* roots from two experiments were used per treatment as indicated. The data are shown as mean ± s.d. The *P* values are from one-way ANOVA with Dunnett's post-test. **e**, Fluo-4-based $[Ca^{2+}]_{cyt}$ response induced by Srf (10 µM) (compared to mock DMSO 0.1%) in root cell protoplasts from Col-0, *mca1/2* and *msl4/5/6/9/10* mutants. The bars indicate mean ± s.d.; the data are grouped from four experiments, with total *n* indicated. The letters indicate significantly different groups at $P < 0.05$ (two-way ANOVA with Tukey's test). **f**, Membrane depolarization visualized by confocal imaging of DiBAC4(3)-stained root epidermal cells from Col-0, *mca1/2* and *msl4/5/6/9/10* mutants treated with Srf (10 µM) compared to mock (DMSO 0.1%). Scale bars, 20 µm. **g**, DiBAC4(3) intracellular fluorescence quantification in root cells. Each dot represents an ROI; total *n* is indicated, and colours denote data from three independent experiments. The box plots show the median and quartiles; the whiskers indicate the range. The *P* values are from two-tailed Mann–Whitney tests. **h**, Disease incidence upon infection by *B. cinerea* in Col-0, *mca1/2* and *msl4/5/6/9/10* mutants pretreated with Srf (10 µM) or mock (EtOH 0.1%). The data points are values obtained for individual plants in two independent experiments with total $n = 30$ for all treatments. The box plots show the quartiles; the whiskers indicate the range. **i**,**j**, Quantification of $[ROS]_{apo}$ burst ($L_{max,15\,min} - L_0$) induced by CO8 in leaves of *msl4/5/6/9/10* (**i**) and *mca1/2* (**j**) mutants pretreated on roots with Srf (10 µM) or mock (EtOH 0.1%). The results are from three independent SIA experiments, and each data point ($n = 3$) is the mean value obtained from 9 to 24 leaf discs in one single experiment. The data are shown as mean ± s.d. The *P* values are from two-tailed *t*-tests. In **a** and **c**, the bars show mean ± s.d., and *n* ROIs were used in total per treatment as indicated. In **a**, **c** and **h**, the *P* values are from two-way ANOVA with Tukey's post-test.

similar to that observed for some anionic amphipathic chemicals[50,51]. We first tested this hypothesis pharmacologically by using the GsMTX-4 peptide as a specific blocker for this type of channel, and we observed severely reduced $[ROS]_{intra}$ and Ca^{2+} burst responses both in root tissues using the HyPer7 biosensor and the *UBQ10*::*GCaMP3* reporter (Fig. 5a,b and Supplementary Video 2) and in protoplasts loaded with DCFH-DA or Fluo4-AM and in Col-0^{AEQ} protoplasts (Extended Data Fig. 9a–c). As expected, this blocker has no or very limited impact on Ca^{2+} signalling by MAMPs or damage-associated molecular patterns, which do not use mechanosensitive ion channels for perception (Fig. 5b and Supplementary Videos 3 and 4), but the general Ca^{2+} channel inhibitor $LaCl_3$ abolished the response for both Srf and flg22 as MAMPs (Extended Data Fig. 9d–f).

Among the stretch-sensitive mechanosensors identified so far in plants, MscS-like 9 (MSL9), MSL10 and Mid1-Complementing Activity 1/2 channels (MCA1/2) are localized in the PM[52,53]. We thus tested the *msl4/5/6/9/10* (ref. 54) quintuple and *mca1/2* (ref. 55) double mutants and observed a significantly decreased responsiveness to Srf in both whole plants and protoplasts (Fig. 5c–e). Importantly, PM depolarization caused by the CLP is also almost abolished in the mutants, meaning that these mechanosensitive gates largely contribute to the related Srf-induced ion fluxes (Fig. 5f,g). In addition, mutant plants were strongly impaired in mounting systemic resistance against pathogen infection (Fig. 5h) or in mounting SIA (Fig. 5i,j), further indicating that functional mechanosensitive channels are necessary for the full response of *Arabidopsis* to Srf elicitation on roots.

Our data provide conclusive evidence for a key role of PM-resident mechanosensors in CLP-induced plant defences. The relative contribution of each channel remains to be determined, as they display specific properties in terms of sensitivity to membrane tension and ion selectivity. MCA1/2 are described as genuine transporters of Ca^{2+} (refs. 53,56), while MSL10 is regarded as a non-selective ion transporter that is indirectly involved in Ca^{2+} signalling upon wounding[57] and response to hyposmotic shock in cell swelling[58]. Both channels may thus act in a coordinated fashion to tailor ion fluxes leading to cellular responses and PM depolarization.

Discussion

As previously reported for other plant species[4], treatment with Srf prepares *Arabidopsis* to mount defence responses culminating in ISR. We now provide molecular insights into CLP-triggered plant immune activation through lipid-mediated detection of these molecules at the cell surface. We propose that sphingolipid-facilitated CLP insertion into the PM remodels membrane structure and organization, resulting in an increase of lateral tension that triggers the activation of PM-localized mechanosensitive ion channels. This allows ion influx and initiates chemical signalling that can be integrated by root cells to activate early immune responses in a process that remains to be deciphered. This lipid-dependent perception at the cell surface may also apply to other bacterial amphiphilic ISR elicitors such as acyl-homoserine lactones and rhamnolipids, which also readily interact with membrane lipids and may thus be perceived via similar mechanisms[4,33,59–61].

PTI works in concert with effector-triggered immunity to provide robust defences against biotrophic invaders, but this canonical immune system is often not efficient against necrotrophic pathogens[8,62]. Here we elucidate a distinct molecular mechanism underlying the activation of ISR in plants, conferring protection against the necrotrophic pathogen *B. cinerea*. This mechanism operates independently of the classical plant immune pathways—PTI and effector-triggered immunity—and also diverges from the Toll-Like-Receptor-dependent recognition of LPs in metazoans[63]. Our findings offer compelling new insights into plant–microbe interactions, highlighting how small bioactive molecules produced by beneficial bacteria can orchestrate robust immune responses in plants. Srf perception leads to a specific immune activation signature regarding the type, timing and amplitude of early defence-related events and a weak transcriptional reprogramming compared with PTI. These findings support the notion that immune activation by Srf does not incur a growth–defence trade-off[64,65]. From an applied perspective, we propose that CLP-induced resistance represents a promising biological alternative to conventional chemical defence enhancers, offering a sustainable strategy for crop protection in agriculture.

Methods

Detailed protocols for LP production and purification, protoplast isolation from root cells, membrane lipidomics, viability tests and liposome preparation are provided in Supplementary Methods. These also contain additional information related to calcium influx and ROS measurements in protoplasts, camalexin quantification, ITC data processing and MD as indicated.

Plant material and growth conditions

Arabidopsis thaliana ecotype Columbia (Col-0) was used as a wild-type control for all plant assays. All mutants used in this study (*fls2 efr1*, *bak1-5*, *bkk1-1*, *bak1-5 bkk1-1*, *bik1 pbl1*, *cerk1-2*, *sobir1-12*, *sobir1-13*, *dorn1-1*, *lore-5*, *pad3*, *rbohd*, *loh1*, *moca1*, *msl4/5/6/9/10* and *mca1/2*) and the reporter lines Col-0^{AEQ}, *R-GECO1* and *UBQ10::GcaMP3* were described previously[19,43,54,55,66–74]. To monitor $[ROS]_{intra}$ accumulation, *A. thaliana* lines expressing the genetically encoded biosensor HyPer7-cyto[22] were used. The HyPer7-cyto sensor was introgressed into mutant backgrounds (*moca1*, *loh1*, *msl4/5/6/9/10* and *mca1/2*) through genetic crosses and floral dip transformation. Briefly, homozygous mutant lines were crossed with the HyPer7-expressing line, and F_2 progeny were screened for homozygous mutants carrying the sensor. For higher-order mutants (*msl4/5/6/9/10* and *mca1/2*), floral dip transformation was performed using *Agrobacterium tumefaciens* (GV3101) carrying the HyPer7-cyto construct, and T_2 progeny were screened for homozygous mutants carrying the sensor.

Seeds were disinfected for 2 min in 75% ethanol and 6 min in 5% bleach and rinsed three times in sterilized water. For $[ROS]_{apo}$, $[ROS]_{intra}$ and protoplast isolation, *Arabidopsis* seeds were grown on half-strength Murashige and Skoog (MS) medium (M0222, Duchefa Biochimie) with the addition of 1% (w/v) sucrose and 14 g l^{-1} of agar, for 2 weeks. For ISR, SIA, alkalinization and conductivity experiments, 1-week-old seedlings, germinated on half-strength MS medium containing 1% (w/v) sucrose and 14 g l^{-1} of agar, were transferred to Araponics systems containing growth solution (0.25% (v/v) FLORAMICRO, 0.25% (v/v) FLORABLOOM, 0.25% (v/v) FLORAGRO; General Hydroponics) (in a volume ratio of 1:1:1, as recommended by the manufacturer), where they were grown for 4 weeks with a photoperiod of 12 h (100 µmol s^{-1} m^{-2}) and a temperature of 23 °C. For the other experiments, growth conditions are specified in the corresponding method sections. For N^+-BODIPY imaging on roots, seedling growth conditions were as previously described[48].

ISR assays

Plants grown for 4 weeks in hydroponics (Araponic systems) were transferred in 10-ml vials filled with fresh nutrient solution and treated at the root level with Srf or other LPs (10 µM) or EtOH 0.1% (mock). After incubation for 24 h, the plants were inoculated with *B. cinerea* using a highly concentrated spore suspension to optimize disease incidence. Spores were collected from *B. cinerea* grown on PDA plates for 4 weeks using a solution composed of 1.75 g l^{-1} KH_2PO_4, 0.74 g l^{-1} $MgSO_4$, 4 g l^{-1} glucose and 0.02 % (v/v) Tween 20. Spore concentration was adjusted to 5 ×105 cells per ml, and suspensions were incubated (30 °C, 180 RPM) for 8 h to favour pre-germination. Infection was performed by applying a drop of 5 µl of spore suspension onto seven leaves per plant. Disease incidence was determined by counting the number of spreading lesions occurring 96 h post-infection per individual plant out of seven infection sites.

SIA assays

SIA was tested on plants like those used for ISR in the same set-up as described above. Four-week-old plants were transferred individually to fresh nutritive solution containing Srf at 10 µM or DMSO 0.1% as a mock treatment and incubated overnight for approximately 16 h. Systemic immune response of elicited plants was then assessed by measuring $[ROS]_{apo}$ burst in leaf tissues upon MAMP perception via a luminol-based chemiluminescence assay adapted from ref. 75. To that end, discs (3 mm Ø) were collected from the fourth and fifth leaves and individually placed into wells of a 96-well white microplate (Lumitrac, Greiner Bio-One) containing 150 µl of water. The plate was incubated at room temperature in the dark overnight. The water was then removed and replaced with 90 µl of fresh deionized water before adding 10 µl of a solution containing 200 µM luminol L-012 + 10 µg ml^{-1} horseradish peroxidase. Luminescence signal was measured using a Spark Tecan multiplate reader. Background luminescence level was measured every minute for 15 min before MAMP treatment and every minute for 60 min after adding CO8 (Elicityl) or flg22 (GenScript) at final concentrations of 2 µM or 1 µM, respectively (with water as a control). The results are expressed as per cent luminescence increase by dividing the measurement at each time point by the measurement at time 0 for each well.

ROS measurements

Measurement of $[ROS]_{apo}$ in *Arabidopsis* roots was performed via the luminol-based chemiluminescence assay. Roots from ten plantlets were pooled per sample before being cut into small pieces and transferred into microplate wells. $[ROS]_{apo}$ production was then quantified upon the addition of Srf, chitin or flg22 at final concentrations of 10 µM, 100 µg ml^{-1} or 1 µM, respectively, or water (mock). The results are expressed as per cent luminescence increase by dividing the measurement at each time point by the measurement at time 0 for each well.

For $[ROS]_{intra}$ measurement in roots with DCFH-DA, 15-mm-long *Arabidopsis* root segments, isolated from different plants, were placed in wells (one root per well) of a microplate (96 Flat Black; Greiner Bio-One CellStar, Fischer Scientific) filled with sterile H_2O. After overnight resting, the roots were incubated with 25 µM DCFH-DA (ACROS Organics) for 20 min and rinsed with PBS before the addition of Srf CLP or mock (water) solutions. Experiments with the channel blockers included an additional step where $LaCl_3$ (10 mM; Sigma-Aldrich) or GsMTX-4 (7.5 µM; MedChemExpress) was added 15 min before treatments. Fluorescence measurements (excitation filter at 485 ± 20 nm and emission filter at 535 ± 25 nm) were performed with a Spark (Tecan) microplate reader using nine readings per well. Data expressed as relative fluorescence increase were obtained by subtracting the fluorescence measured at 0 min from the fluorescence measured at each time point. The fluorescence fold increase was defined for each repeat as the ratio between the fluorescence increase obtained at one time point for treatments and the mean fluorescence increase obtained at the same time point in mock-treated tissues. $[ROS]_{intra}$ measurement in protoplasts is detailed in Supplementary Methods.

Confocal microscopy and image processing for $[ROS]_{intra}$ measurements using the biosensor HyPer7-cyto were performed as follows. Roots from 2- to 3-week-old *Arabidopsis* expressing this biosensor were treated with 10 µM Srf, 1 µM flg22 or 0.1% EtOH (mock) for 25–30 min. $[ROS]_{intra}$ accumulation was visualized using a ZEISS LSM 880 confocal laser scanning microscope with a ×20 objective. The HyPer7-cyto sensor was excited at 488 nm (oxidized form) and 405 nm (reduced form), with emission collected between 508 and 535 nm. The 488/405 nm fluorescence ratio was calculated to determine ROS levels, with acquisition parameters kept consistent across experiments and normalized to the average ratio under control conditions. The fluorescence intensity reflects changes in the HyPer7 sensor ratio (488/405 nm) signal in response to ROS, and a higher HyPer7-cyto ratio thus represents $[ROS]_{intra}$ accumulation. For each experiment, 10–12 ROIs per image were randomly selected for quantification. Signal quantification and ratiometric image analysis were performed using Fiji v2.17.0 (ref. 76).

Calcium influx measurements

Cytosolic Ca^{2+} influx ($[Ca^{2+}]_{cyt}$) was measured in some assays via aequorin-expressing reporter lines (Col-0^{AEQ}). For measurements in root tissue, seeds were sterilized with 75% EtOH and grown on half-strength MS agar plates upright under a 16-h photoperiod for 16 to 20 days. Roots were cut, pooled in wells of white flat-bottom 96-well plates (Lumitrac, Greiner Bio-One) and incubated in 100 µl of 20 µM coelenterazine-h (p.j.k. GmbH) for 5 h in the dark. Luminescence was measured for 2 min before treatment and 30 min after treatment (10 µM Srf, 1 µM flg22 or 100 µg ml^{-1} chitin, or water as mock) by scanning two rows at a time in 10 -s intervals using a Luminoskan Ascent 2.1 luminometer (Thermo Fisher Scientific). Each well was discharged for normalization by the addition of 150 µl of discharge solution (2 M $CaCl_2$ in 20% EtOH), and luminescence was normalized to total luminescence counts remaining (L/L_{max}) to obtain $[Ca^{2+}]$cyt. The method based on Col-0^{AEQ} was adapted for calcium response in root cell protoplasts and is described in Supplementary Methods, together with the method using the Fluo-4 AM probe.

Ca^{2+} influx in roots was captured at high resolution using the R-GECO1 sensor[26,27]. For optimal and undisturbed imaging conditions, plant cultivation chambers were prepared using the commercially available x-well cell culture chambers from Sarstedt (one well, fixed on a cover slide) and 3D-printed three-well combs made from polyethylene terephthalate glycol[77]. Cultivation chambers were assembled by placing one comb per chamber and subsequently positioning a fitted piece of 1/2 MS agar (+0.8% plant agar and 1% sucrose) on top. Seeds were sterilized with ethanol and 6% bleach solution and subsequently stratified at 4 °C in the dark for 3 days prior to seeding. One seed was placed per comb well at the top of the agar slab. The seedlings were grown for 7 days at 22 °C (16-h photoperiod). On the day of imaging, to provide treatment access, the chambers were opened, and the agar below the root tip was cut and discarded. R-GECO1 fluorescence imaging was performed with a high-resolution, inverted, OpenFrame-based epifluorescence microscope (Cairn GmbH), equipped with a ×25 NA1.1 CFI APO LWD objective (Nikon), laser launch (LDI 89 North) and a Teledyne Photometrics Kinetics camera. For imaging, samples were excited with a 577-nm laser (3% intensity), and emission was detected using a 595/26 emission filter. Images were taken every second. Baseline imaging was performed for 3 min, followed by mock (1/2 MS medium and 0.01% DMSO), Srf (10 µM in 1/2 MS and 0.01% DMSO) or flg22 (1 µM) treatment. After 15 min of treatment, a positive control (L-glutamic acid, 1 mM) was added. Imaging data were registered to account for movement of the root. To extract intensity values, ROIs ranging from the root tip to the elongation zone were created using Fiji (https://doi.org/10.1038/nmeth.2019). Intensity values were normalized to the average intensity values of the baseline imaging.

Ca^{2+} influx was also assessed via fluorescence imaging using the *Arabidopsis UBQ10*::*GCaMP3* reporter line[28]. Five-day-old seedlings were grown in round Petri dishes (94 mm Ø) containing 10 ml of sterile 1/2 MS supplemented with 1% (w/v) sucrose and 1% (w/v) agarose. Fluorescence signals (470 nm excitation, 535 nm emission) were monitored as previously described[28], using a Nikon SMZ1270 stereomicroscope (Nikon). To establish the baseline fluorescence, a 2-min video (0.5 fps) was recorded before elicitation for each root. Then, 5 µl of solution of 10 µM Srf or 0.1% DMSO as mock was applied at the root tip of the seedlings. The response to Srf was compared to the one induced by treatment with CO8 (1 µM), flg22 (1 µM) and $OG_{DP10\text{-}15}$ (100 µg ml^{-1}) or water as a control. Ca^{2+} influx dynamics were recorded for 6 min (0.5 fps), and fluorescence signals were analysed in an ROI located approximately 0.3 cm from the root tip and then normalized using the equation $\Delta F/F_0 = (F - F_0)/F_0$, where F represents the fluorescence measured at

each time point and F_0 represents the baseline fluorescence calculated as the average of F over the first 2 min prior to treatments. Images at 0, 60 and 120 s were extracted and pseudo-coloured with fixed LUTs. Data and image processing were performed using NIS-Elements imaging software (Nikon).

Medium alkalinization

Plants were placed in six-well microplates with roots submerged in the same hydroponic solution used for growth in Araponics systems and were treated with 10 µM Srf or 0.1% EtOH as mock. The change in pH was measured with a pH microelectrode (Jenco).

PM depolarization

For experiments on root tissues, *Arabidopsis* seeds were surface-sterilized with EtOH, sown into solid 1/2 MS medium and grown for 5 to 7 days with a 16-h photoperiod. A 10 mM stock solution of Srf was prepared in 100% ethanol the day of the experiment and was diluted to 1:1,000 in liquid 1/2 MS prior the experiment. Staining, treatments and washes were all done in liquid 1/2 MS. *Arabidopsis* seedlings were stained for 15 min with 6.25 µM DiBAC4(3) (Thermo Fisher), followed by two washes. The seedlings were then mounted between a slide and a coverslip in either 0.1% EtOH (mock) or 10 µM Srf to be imaged immediately. *Arabidopsis* roots were imaged with an inverted Zeiss LSM880 equipped with a ×40 objective (NA 1.2, water immersion). The excitation was done at 514 nm, and the detection was done at 517–571 nm. Image analysis was done in Fiji[76], and the mean fluorescence intensity was measured in the cytoplasm of one to three cells per seedling. We observed 18 to 25 seedlings for each condition over the course of three independent experiments.

For assays on protoplasts, we allowed freshly prepared protoplast suspensions (approximately 2 ×105 protoplasts per ml) to rest for 2 h before adding the DiBAC4(3) probe at 2 µM and staining for 15 min. Fluorescence intensity measurements were first performed on 50-µl protoplast aliquots per well of 96-well black microplates. Five microlitres of either DMSO (mock) or Srf was added to each well at final concentrations of 0.1% and 10 µM, respectively. The fluorescence was recorded every 50 s until stable values using a Spark microplate reader (Tecan) with an excitation filter at 485/20 nm and an emission filter at 535/25 nm. Microscopy imaging to evaluate the proportion of stained protoplasts was performed on similar suspensions using a Nikon Ti2-E inverted microscope (Nikon) equipped with 320/0.45 NA S Plan Fluor objective lenses (Nikon) and a Nikon DS-Qi2 monochrome microscope camera. Images taken in the bright-field channel were acquired using a Ti2 Illuminator-DIA and an exposure time of 20 ms.

Electrophysiology

Patch-clamp experiments were performed at room temperature with a patch-clamp amplifier (RK400, Biologic) and a micro1401 digitizer (CED). Currents were filtered at 1 kHz, digitized at 5 kHz, recorded and analysed using WinEDR (v.4.1.6, J. Dempster, Strathclyde University). Isolated protoplasts were maintained in bathing medium: 50 mM $CaCl_2$, 5 mM $MgCl_2$, 10 mM Tris-Hepes and 0.25 mM $LaCl_3$ (pH 5.6) (adapted from ref. 78). The pipettes were filled with 150 mM KCl, 2 mM $MgCl_2$ and 10 mM Tris-Hepes (pH 7.2). Osmolarity was adjusted with mannitol to 584 mOsmol for the bath solution and 640 mOsmol for the pipette solution. Gigaohm resistance seals between pipettes (pipette resistance 5–8 MΩ) pulled from capillaries (GC150F10, Harvard Apparatus), and the protoplast membranes were obtained with gentle suction. Data were recorded using the outside-out configuration, and the membrane potential was clamped at −120 mV. Records were made continuously before, during and after Srf perfusion (10 µM). The data are shown as mean current, which refers to the total current flowing across the membrane patch at a given time. We averaged the current over 10-s intervals to obtain a representative mean value. This corresponds to the classical definition $I_m = N \times P_o \times i$, where I_m is the mean current, N is the number of channels under the patch pipette, P_o is their open probability (which may vary during Srf stimulation) and i is the unitary current according to Ohm's law ($i = g \times V_{hold}$).

Conductivity

Eight-week-old plants grown in Araponics conditions were transferred in 10-times-diluted MS and allowed to rest overnight. Thirty-five millilitres of medium was then collected and supplemented with 10 µM Srf, 0.9% (v/v) Triton X-100 (positive control) or 0.5% (v/v) EtOH (mock treatment). The root of one plant was then immersed in these solutions, and conductivity was measured using a compact conductivity meter LAQUAtwin-EC-33 (HORIBA Scientific).

RNAseq experiments

Plants were grown and treated and RNA was isolated according to ref. 30. Briefly, plant roots were treated with 10 µM Srf or water (mock) for 0, 0.5, 1, 3 and 6 h, with each treatment including three samples, each containing eight roots from different plants. At the end of the treatment, the samples were flash-frozen in liquid nitrogen and stored at −80 °C until the day of RNA extraction. Frozen tissue was homogenized using Eppendorf pestles, and RNA extraction was then conducted using the Plant RNeasy Plant Mini Kit (Qiagen). The sequencing data were processed using the seq2science RNAseq workflow[79]. In short, paired-end reads were first trimmed with fastp v1.0 (ref. 80). Trimmed reads were aligned using STAR v2.7.11b[81] to the *A. thaliana* reference genome (TAIR-10.1). Transcript abundances were then quantified with Salmon[82] using the latest *Arabidopsis* genome annotation (Araport11_GTF_genes_transposons). Finally, differential expression analysis was performed with PyDESeq2 (implementation of DESeq2 v1.34.0)[83] using the significance parameters $P < 0.05$ and $\log_2$(fold change) > 1.

RT–qPCR experiments

For RT–qPCR analysis, plants were grown for 12 days on 1/2 MS supplemented with 1% (w/v) sucrose and 1% (w/v) agar. Seedlings were then transferred individually to 12-well plates containing Araponics growth solution and grown for 10 additional days in these conditions. Fresh medium was added the day before treatment. Study of transcriptional change induced by the treatments was performed according to ref. 30. Briefly, 22-day-old seedlings were treated with 10 µM Srf, 100 µg ml^{-1} chitin or 0.1% EtOH (mock) for 6 h. Each treatment consisted of three samples each containing eight roots. RNA was extracted as described above. RT–qPCR reactions were conducted using the Luna Universal One-Step RT–qPCR Kit (New England Biolabs) following the manufacturer's instructions. The thermal cycling program applied on the ABI StepOne was as follows: 55 °C for 10 min, 95 °C for 1 min, 40 cycles of 95 °C for 10 s and 60 °C for 1 min, followed by a melting curve analysis performed using the default program of the ABI StepOne qPCR machine (Applied Biosystems). The RT-PCR amplification was run on the ABI step-one qPCR instrument (Applied Biosystems) with software version 2.3. The primers used are listed in Supplementary Table 2. The relative gene expression analysis was conducted using the $2^{-\Delta\Delta Ct}$ method with the *UBQ5* gene[84] as a housekeeping gene to normalize mRNA levels between different samples.

Camalexin quantification

Camalexin was quantified in plants obtained from ISR experiments and treated with 10 µM Srf or 0.1% EtOH as mock 96 h after *B. cinerea* inoculation. Each sample (three samples per treatment) contained five plants (only rosette leaves) pooled together. Plant material was flash-frozen with liquid nitrogen, and approximately 100 mg was taken for the extraction. Next, the samples were diluted in 1 ml of 80% methanol, agitated (using a bench rotating agitator) at room temperature in the dark for 2 h and centrifuged (15,160 *g*). The supernatant was dried in a rotational vacuum concentrator (2–25 CDplus, Christ) at 50 °C, and the pellet was resuspended in 1 ml of 100% methanol and shaken again

for 1 h. After centrifugation at 15,160 *g*, the supernatant was combined with the first one for evaporation. The dry powder was resuspended in 1 ml of 100% methanol. The samples were then filtered through 0.2-µm PTFE filters before LC-MS-based quantification as detailed in Supplementary Methods.

ITC

ITC experiments were performed with a VP-ITC Microcalorimeter (Microcal). The calorimeter cell (with a volume of 1.4565 ml) was filled with a 10 µM Srf solution in buffer (Tris 10 mM, NaCl 150 mM at pH 8.5). The syringe was filled with a suspension of LUVs at a lipid concentration of 2 mM (for PLPC–Sito–GluCer composition) or 5 mM (for PLPC, PLPC–Sito and PLPC–GluCer compositions). A series of 10-µl injections was performed at constant time intervals (6 min) at 26 °C. The solution in the titration cell was stirred at 305 r.p.m. Prior to each analysis, all solutions were degassed using a sonicator bath. The heats of dilution of vesicles were determined by injecting vesicles in buffer and subtracted from the heats determined in the experiments. The data were processed using Origin v.7 (Originlab). See Supplementary Methods for the determination of thermodynamic parameters.

MD simulation

An overview of all the simulations performed is presented in Supplementary Table 3. Srf with a C_{14} fatty acid chain was studied via MD in the presence of membranes of PLPC–Sito–GluCer (60–20–20 mol%) with Gromacs v.2020.4 (ref. 85). AT simulations were performed with the CHARMM36 force field[86]. Membrane systems of 140 and 180 lipids were generated using the CHARMM-GUI membrane builder[87] and the box filled with TIP3P water[88] with a KCl concentration of 150 mM. Further details on systems equilibration are provided in Supplementary Methods. Membrane-only systems were first equilibrated for 500 ns. For Srf insertion simulations, one Srf molecule was placed at least 2 nm above the bilayer surface of the 140 lipid membranes, while for the other simulations, the Srf molecules were first inserted in the 180 lipid membranes through a pulling step on the last carbon of the Srf acyl chain. For insertion simulations, six replicas were carried on for 2.5 µs or until the Srf insertion was completed. For the other simulations, three replicas were carried on with Srf preinserted in the upper leaflet at an LP/lipid ratio of 0.05 and simulated for 1 µs or preinserted in both leaflets at a ratio of 0.1 or 0.05 and simulated for 0.5 and 1 µs, respectively. CG simulations were carried out with the MARTINI 3 forcefield[89]. The atomistic Srf model was converted to a CG representation with the Martinize script, and the membranes were built with the insane tool[90]. Further details on settings are provided in Supplementary Methods. Membrane systems were first equilibrated for 10 µs. The Srf molecules were then inserted in the membrane through a pulling step on the last bead of the Srf acyl chain. Srf molecules were preinserted in the upper leaflet at a ratio of 0.016 and simulated for 5 µs or preinserted in both leaflets at a ratio of 0.032 and simulated for 20 µs. Trajectories were performed and analysed with GROMACS v.2020.4 tools[91], MDAnalysis v2.8.0 (ref. 92), Lipyphilic v0.11.0 (ref. 93), PackMEM v1.0 (ref. 94) and LipidDyn v0.3 (ref. 95). For the AT simulations, the first 100 ns of simulation were not considered. For the CG simulations, the simulations were divided into four blocks of equivalent length, and the last three were used as independent simulations for the statistical analysis. For radial distribution functions, curves were first smoothed over 1 Å. Radial distribution functions were computed by following representative particles for Srf and each lipid: the lactone for Srf, the phosphate for PLPC, the hydroxyl for Sito and the amide for GluCer. 3D structures were analysed with both PYMOL v2.5.0 (ref. 96) and VMD v1.9.3 (ref. 97).

NR

The SLD of the Srf mixture was calculated according to relative molar proportions, by considering a volume of 1,143 $Å^3$ for the hydrophilic portion and 373 $Å^3$ for the fatty acid[49,98] (Extended Data Table 1 and Supplementary Table 4). Lipid bilayer (ternary mixture of PLPC–Sito–GluCer, 60–20–20 mol%) depositions on silicon for NR measurements were obtained by injecting the LUVs directly into the measuring cell (6 ml) at room temperature to a final concentration of 0.5 mg ml^{-1}, according to the procedures described in ref. 99.

NR data were acquired at the MARIA neutron reflectometer[100] operated by the Jülich Centre for Neutron Science at Heinz Maier-Leibnitz Zentrum in Garching, Germany, using custom temperature-regulated liquid cells[101]. The measurements were performed using two different wavelengths, 10 Å for the low-q region and 5 Å for the high-q region up to 0.25 $Å^{-1}$, with a 10% wavelength spread. The change of solvent contrast in the liquid cells was performed using a combination of valves and a peristaltic pump, at small flow rates ~0.5 ml min^{-1}. In an NR experiment, a grazing beam is sent to the sample, and the reflected intensity is collected as a function of the reflection angle momentum transfer perpendicular to the interface qz ($qz = 4\lambda\sin(\vartheta/2)$, where ϑ and λ are the angle of the incident beam and wavelength, respectively). The technique allows one to get information about the sample cross structuring in a non-invasive way[102,103]. The silicon oxide layer, the water layer between the silicon oxide and the membrane and the different hydrophilic and hydrophobic layers of the lipid membranes were modelled as defined layers with a proper thickness, compactness and mean composition (and therefore neutron SLD). Reflectivity was measured from the silicon supports and the samples in different water solutions (H_2O and D_2O; Sigma Chemical Co.). After bare membrane characterization in two solvents, a buffer of 10 mM Tris and 150 mM NaCl at pH 8.5 solution was injected into the cell, and NR measurement was performed. Finally, 2 µg of Srf in Tris HCl buffer at pH 8.5 was injected into the cell, to a final membrane:Srf molar proportion of 95:5 (Srf final concentration, 0.24 µM). NR measurements were performed on this system after 30 min of incubation. The data were analysed using the MotoFit program[104]. Data relative to the same system measured in different water contrasts were analysed using contemporary fits.

SAXS and WAXS

LUVs (PLPC–Sito–GluCer (60–20–20 mol%)) were separated on two aliquots: to the first, the required volume of Srf solution in buffer was added to obtain a final lipid-to-Srf molar proportion of 95–5, while the second was diluted with the same amount of pure buffer.

SAXS/WAXS investigations were performed at the ID02 beamline of the European Synchrotron (ESRF). The sample-to-detector distance for SAXS was 1 m to cover a **q**-range, $0.07 < \mathbf{q} < 5$ nm^{-1}, where **q** is the scattering wave vector defined as $\mathbf{q} = (4\pi/\lambda)\sin(\vartheta/2)$, where λ is the wavelength ($\lambda \approx 1$ Å) and ϑ is the scattering angle. Measurements were performed using polycarbonate capillaries of 2 mm thickness (ENKI) as sample containers. The measured patterns were corrected for detector artefacts, normalized and azimuthally averaged to obtain the intensity profile $I(\mathbf{q})$ using standard procedures[105]. For each sample, 10 frames were acquired and subsequently averaged after excluding any possible radiation damage. The background scattering of the buffer was also measured. The averaged background signal was subtracted from each averaged sample scattering intensity profile, and best fits for the measured data were obtained by modelling the membrane with four Gaussians, with two Gaussians centred in the membrane centre, to account for the lipid chains, and two Gaussians to account for the two headgroup layers.

AFM experiments

Supported lipid bilayers (ternary mixture of PLPC, Sito and GluCer at 60–20–20 mol%) were reconstructed on freshly cleaved mica substrates by allowing the fusion of a 2 mM LUV solution ($V = 100$ µl) at 55 °C for 45 min. The samples were then let for thermalization at ambient temperature for 30 min without dewetting and immersed in 3 ml of 10 mM Tris and 150 mM NaCl buffer at pH 8.5. To avoid damaging the samples, AFM images were obtained in the quantitative imaging

mode of a JPK Nanowizard III set-up, with a minimal applied force of 200 pN and a speed of 50 µm s^{-1}. Soft sharpened silicon nitride cantilevers (MSCT, Bruker) were used and calibrated before any experiment using the thermal noise method ($k \approx 0.02$ N m^{-1}). Srf, prepared in 10 mM Tris and 150 mM NaCl buffer at pH 8.5, was finally injected at a final concentration of 3 µM. AFM images were then recorded at different time points in different areas to follow its impact on the lipid bilayer.

DLS measurements on liposomes

DLS measurements were performed on LUV solutions (300 µM) at different concentrations of Srf (0, 10, 20, 40 and 75 µM). The scattered intensity was measured at 25 °C using a Zetasizer Nano DLS instrument with a He–Ne laser source at a wavelength of 633 nm (Malvern Panalytical) to obtain the liposome size and the derived count rate, in kilo counts per second. After an initial measurement to get LUV size and derived count rate without Srf, Srf from a stock solution of 10 mM in EtOH was successively added in the liposome solution to obtain the evolution of LUV size with increasing Srf concentration. Measurements were performed three times on each sample to ensure reproducibility (eight acquisitions per measurement with an acquisition time of 10–15 s).

FRET measurements

Wells of black 96-well microplates (Greiner Bio-One CellStar, Fischer Scientific) were loaded with 190 µl of LUV solution (0.2 mM) per well. The fluorescence was recorded using a Spark microplate reader (Tecan) by performing a fluorescence scan between 515 and 650 nm (bandwidth, 20 nm) with an excitation wavelength at 470 nm (bandwidth, 20 nm). The FRET efficiency (E) was calculated on the basis of the measurement of energy transfer from donor (D) emission (541 nm) with the formula:

$$E = 1 - \frac{A_D}{A_{DA}} \frac{I_{DA}}{I_D}$$

where A_D and A_{DA} are the donor absorbances at the excitation wavelength in the donor-only and donor + acceptor samples, respectively, and I_{DA} and I_D are the donor fluorescence intensities in the presence and absence of the acceptor, respectively.

For the PLPC–Sito–GluCer system, the fluorescence was recorded once before treatment and at various times after the addition of 10 µl of treatment (Srf at a final concentration of 10 µM or 0.1% EtOH as mock). Srf solution was initially prepared at 10 mM in EtOH and diluted at 200 µM in 10 mM Tris and 150 mM NaCl buffer at pH 8.5.

Laurdan polarization on root protoplasts and lipid vesicles

Protoplast suspension (1–2 × 10^5 protoplasts per ml) or 100 µM LUV preparation was incubated with 2 µM Laurdan (Sigma-Aldrich) for 1 h. The wells of black 96-well microplates (Greiner Bio-One CellStar, Fischer Scientific) were then loaded with 100 µl of protoplasts or LUV solution per well. The fluorescence was recorded using a Spark microplate reader (Tecan) by performing a fluorescence scan between 405 nm and 520 nm with an excitation wavelength at 360 nm. The fluorescence was recorded once before treatment and at various times after the addition of 25 µl (for protoplasts) or 100 µl (for LUVs) of treatment (the final concentration of Srf was 10 µM; DMSO at a final concentration of 0.1% corresponds to mock). The treatments were prepared in the buffer of protoplasts (WI_{Ca} solution) or LUV buffer, respectively, with a concentration taking into account the dilution factor occurring at the addition of treatment into 100 µl of protoplasts or LUV solution (five times more concentrated for protoplasts and two times more concentrated for LUVs). The GP was defined as

$$GP = \frac{(I_{440nm} - I_{490nm})}{(I_{440nm} + I_{490nm})},$$

where I_{440nm} and I_{490nm} represent the blank-subtracted fluorescence intensities at emission wavelengths of 440 nm and 490 nm, respectively. For measurement after Srf treatment, GP values were calculated on data at 5 min after the addition of Srf treatment.

FLIM of Flipper-TR on protoplasts

First, 100 µl of protoplast suspension previously incubated with 2 µl of Flipper-TR at 1 mM in DMSO was added on the bottom of an IBIDI chamber (pretreated with BSA at 4 °C for 1–2 h and washed twice with 300 µl of WI_{Ca}). The slide was centrifuged at 200 g for 5 min. Then, 50 µl of WI_{Ca} was replaced by 50 µl of Srf at 20 µM (prepared in WI_{Ca} from a stock solution in DMSO; Srf image) or 50 µl of DMSO-matched WI_{Ca} (DMSO image)) and imaged for 30 min. The isosmotic control (control image) corresponds to the protoplast sample in WI_{Ca} with no treatment. Hyposmotic protoplast samples (high-tension image) were prepared in the same way but replacing 200 µl of the 300 µl of WI_{Ca} in the IBIDI cell with 200 µl of pure water. For hyperosmotic protoplast samples (low-tension image), 200 µl of the 300 µl of WI_{Ca} in the IBIDI cell was replaced with 200 µl of WI_{Ca} supplemented with 200 mM NaCl.

FLIM of Flipper-TR was performed with an LSM980 microscope (Zeiss) equipped with a time-correlated single photon counting FLIM module (PicoQuant). Flipper-TR in root protoplasts was excited with a Coherent (Chameleon Discovery) pulsed laser (80 MHz) at 960 nm. The emission was recorded with a bandpass filter (570–610 nm) at a resolution of 512 × 512 pixels. All images were acquired with a Plan-Apochromat ×63/1.4 oil-immersion objective. The analysis of the FLIM images was performed with SymPhoTime64 (PicoQuant), which allows fitting the fluorescence decay of the image pixels to mathematical decay models and obtaining the FLIM fit images directly on screen. Furthermore, the production of intensity coded lifetime and histograms was done with a home-written MATLAB routine that has been used multiple times[106].

FLIM of N^+-BODIPY on *Arabidopsis* roots

A 10 mM stock solution of Srf was prepared in ethanol the day of the experiment and was diluted to 1:1,000 in liquid 1/2 MS prior the experiment. Staining, treatments and washes were all done in liquid 1/2 MS. *Arabidopsis* seedlings were stained for 15 min with 10 µM N^+-BODIPY, followed by two washes. The seedlings were then mounted between a slide and a coverslip in either 0.1% ethanol or 10 µM Srf to be imaged immediately. Roots were imaged with an inverted Leica SP8 equipped with a ×40 objective (water immersion). The excitation was done with a pulse laser (40 Hz repetition) at 470 nm, and fluorescence collection was done at 510–530 nm until 1,000 photons per pixel were collected. FLIM acquisition and integration was done with PiqoQuant Symphotime. One to three ROIs per seedling were used for lifetime fitting. Lifetime fitting was done using a two-component exponential reconvolution. Statistical analysis and plotting were done in R v4.5.2 (ref. 107) (wilcox.test).

GP imaging of C-Laurdan on GUVs

First, 90 µl of GUV suspension previously mixed for 20 min with 10 µl of Srf (dispersed in 10 mM Tris and 150 mM NaCl buffer at pH 8.5 from a stock solution in ethanol to obtain an Srf final concentration of 5, 10 or 20 µM) or control buffer (ethanol-matched) was incubated for 10 min (37 °C) with 30 µl of 5 µM C-Laurdan. C-Laurdan, which reports membrane packing close to the membrane interface, is a more photostable derivative of the Laurdan probe and is therefore more suitable for confocal microscopy. The mixture was added on the bottom of an IBIDI chamber (pretreated with BSA at 4 °C for 1–2 h and washed twice with 300 µl of buffer). The slide was centrifuged at 150 g for 5 min prior to fluorescence imaging. GP imaging of C-Laurdan was performed with an LSM980 microscope (Zeiss) equipped with a time-correlated single photon counting FLIM module (PicoQuant). C-Laurdan was excited with a 405-nm laser, and emission was recorded in two spectral

windows with maxima at 440 and 490 nm. All images were acquired with a Plan-Apochromat ×63/1.4 oil-immersion objective. The production of GP images and histograms was done with a home-written MATLAB routine that has been used multiple times[106]. In the images, the GUVs systematically display a higher GP in the horizontal plane. This is due to the photoselection effect of Laurdan molecules that are aligned in parallel to the polarization angle of the laser.

Statistics
Statistical details of the experiments are specified in the figure legends. Unless otherwise stated, all statistical analyses were performed in GraphPad Prism v.10.6.1 for Mac[108].

Materials availability
Materials related to all experiments except RNAseq are available via Zenodo at https://doi.org/10.5281/zenodo.8358628 (ref. 109).

Reporting summary
Further information on research design is available in the Nature Portfolio Reporting Summary linked to this article.

Data availability
All data are available within this article and its Supplementary Information. Original data points in graphs related to all experiments except RNAseq are available via Zenodo at https://doi.org/10.5281/zenodo.8358627 (ref. 109). RNAseq data are available via Zenodo at https://doi.org/10.5281/zenodo.10013102 (ref. 110). Source data are provided with this paper.

Code availability
The code used in this study is available via Zenodo at https://doi.org/10.5281/zenodo.8358628 (ref. 109).

References

1. Balleux, G., Höfte, M., Arguelles-Arias, A., Deleu, M. & Ongena, M. *Bacillus* lipopeptides as key players in rhizosphere chemical ecology. *Trends Microbiol.* **33**, 80–95 (2025).
2. Gutiérrez-Chávez, C., Benaud, N. & Ferrari, B. C. The ecological roles of microbial lipopeptides: where are we going? *Comput. Struct. Biotechnol. J.* **19**, 1400–1413 (2021).
3. Mohammad, M. et al. *Staphylococcus aureus* lipoproteins in infectious diseases. *Front. Microbiol.* **13**, 1006765 (2022).
4. Pršić, J. & Ongena, M. Elicitors of plant immunity triggered by beneficial bacteria. *Front. Plant Sci.* **11**, 594530 (2020).
5. Cesa-Luna, C. et al. Charting the lipopeptidome of nonpathogenic *Pseudomonas*. *mSystems* **8**, e00988-22 (2023).
6. Blake, C., Christensen, M. N. & Kovács, Á. T. Molecular aspects of plant growth promotion and protection by *Bacillus subtilis*. *Mol. Plant Microbe Interact.* **34**, 15–25 (2021).
7. Vlot, A. C. et al. Systemic propagation of immunity in plants. *New Phytol.* **229**, 1234–1250 (2021).
8. Zhang, L., Hua, C., Janocha, D., Fliegmann, J. & Nürnberger, T. Plant cell surface immune receptors—novel insights into function and evolution. *Curr. Opin. Plant Biol.* **74**, 102384 (2023).
9. DeFalco, T. A. & Zipfel, C. Molecular mechanisms of early plant pattern-triggered immune signaling. *Mol. Cell* **81**, 3449–3467 (2021).
10. Waszczak, C., Carmody, M. & Kangasjärvi, J. Reactive oxygen species in plant signaling. *Annu. Rev. Plant Biol.* **69**, 209–236 (2018).
11. Köster, P., DeFalco, T. A. & Zipfel, C. Ca^{2+} signals in plant immunity. *EMBO J.* **41**, e110741 (2022).
12. Falhof, J., Pedersen, J. T., Fuglsang, A. T. & Palmgren, M. Plasma membrane H+-ATPase regulation in the center of plant physiology. *Mol. Plant* **9**, 323–337 (2016).
13. Meng, X. & Zhang, S. MAPK cascades in plant disease resistance signaling. *Annu. Rev. Phytopathol.* **51**, 245–266 (2013).
14. Harwood, C. R., Mouillon, J.-M., Pohl, S. & Arnau, J. Secondary metabolite production and the safety of industrially important members of the *Bacillus subtilis* group. *FEMS Microbiol. Rev.* **42**, 721–738 (2018).
15. Cawoy, H. et al. Plant defense stimulation by natural isolates of *Bacillus* depends on efficient surfactin production. *Mol. Plant Microbe Interact.* **27**, 87–100 (2014).
16. Zhou, J. et al. Multilayered synergistic regulation of phytoalexin biosynthesis by ethylene, jasmonate, and MAPK signaling pathways in *Arabidopsis*. *Plant Cell* **34**, 3066–3087 (2022).
17. Ferrari, S., Plotnikova, J. M., De Lorenzo, G. & Ausubel, F. M. *Arabidopsis* local resistance to *Botrytis cinerea* involves salicylic acid and camalexin and requires EDS4 and PAD2, but not SID2, EDS5 or PAD4. *Plant J.* **35**, 193–205 (2003).
18. Denoux, C. et al. Activation of defense response pathways by OGs and flg22 elicitors in *Arabidopsis* seedlings. *Mol. Plant* **1**, 423–445 (2008).
19. Glazebrook, J. & Ausubel, F. M. Isolation of phytoalexin-deficient mutants of *Arabidopsis thaliana* and characterization of their interactions with bacterial pathogens. *Proc. Natl Acad. Sci. USA* **91**, 8955–8959 (1994).
20. Nühse, T. S., Bottrill, A. R., Jones, A. M. E. & Peck, S. C. Quantitative phosphoproteomic analysis of plasma membrane proteins reveals regulatory mechanisms of plant innate immune responses. *Plant J.* **51**, 931–940 (2007).
21. Morales, J., Kadota, Y., Zipfel, C., Molina, A. & Torres, M.-A. The *Arabidopsis* NADPH oxidases RbohD and RbohF display differential expression patterns and contributions during plant immunity. *J. Exp. Bot.* **67**, 1663–1676 (2016).
22. Ugalde, J. M., Schlößer, M., Dongois, A., Martinière, A. & Meyer, A. J. The latest HyPe(r) in plant H_2O_2 biosensing. *Plant Physiol.* **187**, 480–484 (2021).
23. Arnaud, D., Deeks, M. J. & Smirnoff, N. Organelle-targeted biosensors reveal distinct oxidative events during pattern-triggered immune responses. *Plant Physiol.* **191**, 2551–2569 (2023).
24. Shang-Guan, K. et al. Lipopolysaccharides trigger two successive bursts of reactive oxygen species at distinct cellular locations. *Plant Physiol.* **176**, 2543–2556 (2018).
25. Ashtamker, C., Kiss, V., Sagi, M., Davydov, O. & Fluhr, R. Diverse subcellular locations of cryptogein-induced reactive oxygen species production in tobacco Bright Yellow-2 cells. *Plant Physiol.* **143**, 1817–1826 (2007).
26. Keinath, N. F. et al. Live cell imaging with R-GECO1 sheds light on flg22- and chitin-induced transient $[Ca^{2+}]_{cyt}$ patterns in *Arabidopsis*. *Mol. Plant* **8**, 1188–1200 (2015).
27. Wan, W.-L. et al. Comparing *Arabidopsis* receptor kinase and receptor protein-mediated immune signaling reveals BIK1-dependent differences. *New Phytol.* **221**, 2080–2095 (2019).
28. Toyota, M. et al. Glutamate triggers long-distance, calcium-based plant defense signaling. *Science* **361**, 1112–1115 (2018).
29. Liu, B. et al. The anion channel SLAH3 interacts with potassium channels to regulate nitrogen–potassium homeostasis and the membrane potential in *Arabidopsis*. *Plant Cell* **35**, 1259–1280 (2023).
30. Stringlis, I. A. et al. Root transcriptional dynamics induced by beneficial rhizobacteria and microbial immune elicitors reveal signatures of adaptation to mutualists. *Plant J.* **93**, 166–180 (2018).
31. Bjornson, M., Pimprikar, P., Nürnberger, T. & Zipfel, C. The transcriptional landscape of *Arabidopsis thaliana* pattern-triggered immunity. *Nat. Plants* **7**, 579–586 (2021).
32. Kutschera, A. et al. Bacterial medium-chain 3-hydroxy fatty acid metabolites trigger immunity in *Arabidopsis* plants. *Science* **364**, 178–181 (2019).

33. Schellenberger, R. et al. Bacterial rhamnolipids and their 3-hydroxyalkanoate precursors activate *Arabidopsis* innate immunity through two independent mechanisms. *Proc. Natl Acad. Sci. USA* **118**, e2101366118 (2021).
34. Liang, X. & Zhou, J.-M. Receptor-like cytoplasmic kinases: central players in plant receptor kinase-mediated signaling. *Annu. Rev. Plant Biol.* **69**, 267–299 (2018).
35. Albert, I. et al. An RLP23–SOBIR1–BAK1 complex mediates NLP-triggered immunity. *Nat. Plants* **1**, 15140 (2015).
36. Fan, L. et al. Genotyping-by-sequencing-based identification of *Arabidopsis* pattern recognition receptor RLP32 recognizing proteobacterial translation initiation factor IF1. *Nat. Commun.* **13**, 1294 (2022).
37. Henry, G., Deleu, M., Jourdan, E., Thonart, P. & Ongena, M. The bacterial lipopeptide surfactin targets the lipid fraction of the plant plasma membrane to trigger immune-related defence responses. *Cell. Microbiol.* **13**, 1824–1837 (2011).
38. Balleza, D., Alessandrini, A. & Beltrán García, M. J. Role of lipid composition, physicochemical interactions, and membrane mechanics in the molecular actions of microbial cyclic lipopeptides. *J. Membr. Biol.* **252**, 131–157 (2019).
39. Gronnier, J., Gerbeau-Pissot, P., Germain, V., Mongrand, S. & Simon-Plas, F. Divide and rule: plant plasma membrane organization. *Trends Plant Sci.* **23**, 899–917 (2018).
40. Haslam, T. M. & Feussner, I. Diversity in sphingolipid metabolism across land plants. *J. Exp. Bot.* **73**, 2785–2798 (2022).
41. Bahammou, D. et al. A combined lipidomic and proteomic profiling of *Arabidopsis thaliana* plasma membrane. *Plant J.* **119**, 1570–1595 (2024).
42. Ingólfsson, H. I. et al. Lipid organization of the plasma membrane. *J. Am. Chem. Soc.* **136**, 14554–14559 (2014).
43. Ternes, P. et al. Disruption of the ceramide synthase LOH1 causes spontaneous cell death in *Arabidopsis thaliana*. *New Phytol.* **192**, 841–854 (2011).
44. Lenarčič, T. et al. Eudicot plant-specific sphingolipids determine host selectivity of microbial NLP cytolysins. *Science* **358**, 1431–1434 (2017).
45. Gerbeau-Pissot, P. et al. Modification of plasma membrane organization in tobacco cells elicited by cryptogein. *Plant Physiol.* **164**, 273–286 (2014).
46. Sandor, R. et al. Plasma membrane order and fluidity are diversely triggered by elicitors of plant defence. *J. Exp. Bot.* **67**, 5173–5185 (2016).
47. Colom, A. et al. A fluorescent membrane tension probe. *Nat. Chem.* **10**, 1118–1125 (2018).
48. Michels, L. et al. Complete microviscosity maps of living plant cells and tissues with a toolbox of targeting mechanoprobes. *Proc. Natl Acad. Sci. USA* **117**, 18110–18118 (2020).
49. Shen, H.-H., Thomas, R. K. & Taylor, P. The location of the biosurfactant surfactin in phospholipid bilayers supported on silica using neutron reflectometry. *Langmuir* **26**, 320–327 (2010).
50. Martinac, B., Adler, J. & Kung, C. Mechanosensitive ion channels of *E. coli* activated by amphipaths. *Nature* **348**, 261–263 (1990).
51. Hamilton, E. S., Schlegel, A. M. & Haswell, E. S. United in diversity: mechanosensitive ion channels in plants. *Annu. Rev. Plant Biol.* **66**, 113–137 (2015).
52. Demidchik, V., Shabala, S., Isayenkov, S., Cuin, T. A. & Pottosin, I. Calcium transport across plant membranes: mechanisms and functions. *New Phytol.* **220**, 49–69 (2018).
53. Yoshimura, K., Iida, K. & Iida, H. MCAs in *Arabidopsis* are Ca^{2+}-permeable mechanosensitive channels inherently sensitive to membrane tension. *Nat. Commun.* **12**, 6074 (2021).
54. Haswell, E. S., Peyronnet, R., Barbier-Brygoo, H., Meyerowitz, E. M. & Frachisse, J.-M. Two MscS homologs provide mechanosensitive channel activities in the *Arabidopsis* root. *Curr. Biol.* **18**, 730–734 (2008).
55. Yamanaka, T. et al. MCA1 and MCA2 that mediate Ca^{2+} uptake have distinct and overlapping roles in *Arabidopsis*. *Plant Physiol.* **152**, 1284–1296 (2010).
56. Mori, K. et al. Ca^{2+}-permeable mechanosensitive channels MCA1 and MCA2 mediate cold-induced cytosolic Ca^{2+} increase and cold tolerance in *Arabidopsis*. *Sci. Rep.* **8**, 550 (2018).
57. Moe-Lange, J. et al. Interdependence of a mechanosensitive anion channel and glutamate receptors in distal wound signaling. *Sci. Adv.* **7**, eabg4298 (2021).
58. Basu, D. & Haswell, E. S. The mechanosensitive ion channel MSL10 potentiates responses to cell swelling in *Arabidopsis* seedlings. *Curr. Biol.* **30**, 2716–2728.e6 (2020).
59. Schellenberger, R. et al. Apoplastic invasion patterns triggering plant immunity: plasma membrane sensing at the frontline. *Mol. Plant Pathol.* **20**, 1602–1616 (2019).
60. Schikora, A., Schenk, S. T. & Hartmann, A. Beneficial effects of bacteria–plant communication based on quorum sensing molecules of the *N*-acyl homoserine lactone group. *Plant Mol. Biol.* **90**, 605–612 (2016).
61. Davis, B. M., Jensen, R., Williams, P. & O'Shea, P. The interaction of *N*-acylhomoserine lactone quorum sensing signaling molecules with biological membranes: implications for inter-kingdom signaling. *PLoS ONE* **5**, e13522 (2010).
62. Ngou, B. P. M., Ding, P. & Jones, J. D. G. Thirty years of resistance: zig-zag through the plant immune system. *Plant Cell* **34**, 1447–1478 (2022).
63. Jin, M. S. et al. Crystal structure of the TLR1–TLR2 heterodimer induced by binding of a tri-acylated lipopeptide. *Cell* **130**, 1071–1082 (2007).
64. Debois, D. et al. Plant polysaccharides initiate underground crosstalk with bacilli by inducing synthesis of the immunogenic lipopeptide surfactin. *Environ. Microbiol. Rep.* **7**, 570–582 (2015).
65. He, Z., Webster, S. & He, S. Y. Growth–defense trade-offs in plants. *Curr. Biol.* **32**, R634–R639 (2022).
66. Nekrasov, V. et al. Control of the pattern-recognition receptor EFR by an ER protein complex in plant immunity. *EMBO J.* **28**, 3428–3438 (2009).
67. Zhang, J. et al. Receptor-like cytoplasmic kinases integrate signaling from multiple plant immune receptors and are targeted by a *Pseudomonas syringae* effector. *Cell Host Microbe* **7**, 290–301 (2010).
68. Schwessinger, B. et al. Phosphorylation-dependent differential regulation of plant growth, cell death, and innate immunity by the regulatory receptor-like kinase BAK1. *PLoS Genet.* **7**, e1002046 (2011).
69. Miya, A. et al. CERK1, a LysM receptor kinase, is essential for chitin elicitor signaling in *Arabidopsis*. *Proc. Natl Acad. Sci. USA* **104**, 19613–19618 (2007).
70. Leslie, M. E., Lewis, M. W., Youn, J.-Y., Daniels, M. J. & Liljegren, S. J. The EVERSHED receptor-like kinase modulates floral organ shedding in *Arabidopsis*. *Development* **137**, 467–476 (2010).
71. Torres, M. A., Dangl, J. L. & Jones, J. D. G. *Arabidopsis* gp91phox homologues AtrbohD and AtrbohF are required for accumulation of reactive oxygen intermediates in the plant defense response. *Proc. Natl Acad. Sci. USA* **99**, 517–522 (2002).
72. Ranf, S. et al. A lectin S-domain receptor kinase mediates lipopolysaccharide sensing in *Arabidopsis thaliana*. *Nat. Immunol.* **16**, 426–433 (2015).
73. Ranf, S. et al. Defense-related calcium signaling mutants uncovered via a quantitative high-throughput screen in *Arabidopsis thaliana*. *Mol. Plant* **5**, 115–130 (2012).

74. Knight, H., Trewavas, A. J. & Knight, M. R. Cold calcium signaling in *Arabidopsis* involves two cellular pools and a change in calcium signature after acclimation. *Plant Cell* **8**, 489–503 (1996).
75. Albert, M. & Fürst, U. in *Plant Receptor Kinases: Methods and Protocols* (ed. Aalen, R. B.) 69–76 (Springer, 2017); https://doi.org/10.1007/978-1-4939-7063-6_7
76. Schindelin, J. et al. Fiji: an open-source platform for biological-image analysis. *Nat. Methods* **9**, 676–682 (2012).
77. Guichard, M., Holla, S., Wernerová, D., Grossmann, G. & Minina, E. A. RoPod, a customizable toolkit for non-invasive root imaging, reveals cell type-specific dynamics of plant autophagy. *Sci. Rep.* **14**, 12664 (2024).
78. Tran, D. et al. Cellular transduction of mechanical oscillations in plants by the plasma-membrane mechanosensitive channel MSL10. *Proc. Natl Acad. Sci. USA* **118**, e1919402118 (2021).
79. Sande et al. Seq2science: an end-to-end workflow for functional genomics analysis. *PeerJ* **11**, e16380 (2023).
80. Chen, S., Zhou, Y., Chen, Y. & Gu, J. fastp: an ultra-fast all-in-one FASTQ preprocessor. *Bioinformatics* **34**, i884–i890 (2018).
81. Dobin, A. et al. STAR: ultrafast universal RNA-seq aligner. *Bioinformatics* **29**, 15–21 (2013).
82. Patro, R., Duggal, G., Love, M. I., Irizarry, R. A. & Kingsford, C. Salmon provides fast and bias-aware quantification of transcript expression. *Nat. Methods* **14**, 417–419 (2017).
83. Muzellec, B., Teleńczuk, M., Cabeli, V. & Andreux, M. PyDESeq2: a Python package for bulk RNA-seq differential expression analysis. *Bioinformatics* **39**, btad547 (2023).
84. Basu, D., Codjoe, J. M., Veley, K. M. & Haswell, E. S. The mechanosensitive ion channel MSL10 modulates susceptibility to *Pseudomonas syringae* in *Arabidopsis thaliana*. *Mol. Plant Microbe Interact.* **35**, 567–582 (2022).
85. Hess, B., Kutzner, C., van der Spoel, D. & Lindahl, E. GROMACS 4: algorithms for highly efficient, load-balanced, and scalable molecular simulation. *J. Chem. Theory Comput.* **4**, 435–447 (2008).
86. Klauda, J. B. et al. Update of the CHARMM all-atom additive force field for lipids: validation on six lipid types. *J. Phys. Chem. B* **114**, 7830–7843 (2010).
87. Wu, E. L. et al. CHARMM-GUI membrane builder toward realistic biological membrane simulations. *J. Comput. Chem.* **35**, 1997–2004 (2014).
88. Jorgensen, W. L., Chandrasekhar, J., Madura, J. D., Impey, R. W. & Klein, M. L. Comparison of simple potential functions for simulating liquid water. *J. Chem. Phys.* **79**, 926–935 (1983).
89. Souza, P. C. T. et al. Martini 3: a general purpose force field for coarse-grained molecular dynamics. *Nat. Methods* **18**, 382–388 (2021).
90. Wassenaar, T. A., Ingólfsson, H. I., Böckmann, R. A., Tieleman, D. P. & Marrink, S. J. Computational lipidomics with insane: a versatile tool for generating custom membranes for molecular simulations. *J. Chem. Theory Comput.* **11**, 2144–2155 (2015).
91. Abraham, M. J. et al. GROMACS: high performance molecular simulations through multi-level parallelism from laptops to supercomputers. *SoftwareX* **1–2**, 19–25 (2015).
92. Michaud-Agrawal, N., Denning, E. J., Woolf, T. B. & Beckstein, O. MDAnalysis: a toolkit for the analysis of molecular dynamics simulations. *J. Comput. Chem.* **32**, 2319–2327 (2011).
93. Smith, P. & Lorenz, C. D. LiPyphilic: a Python toolkit for the analysis of lipid membrane simulations. *J. Chem. Theory Comput.* **17**, 5907–5919 (2021).
94. Gautier, R. et al. PackMem: a versatile tool to compute and visualize interfacial packing defects in lipid bilayers. *Biophys. J.* **115**, 436–444 (2018).
95. Scrima, S. et al. Unraveling membrane properties at the organelle-level with LipidDyn. *Comput. Struct. Biotechnol. J.* **20**, 3604–3614 (2022).
96. PyMOL Molecular Graphics System v.1.8 (Schrödinger, 2015).
97. Humphrey, W., Dalke, A. & Schulten, K. VMD: visual molecular dynamics. *J. Mol. Graph.* **14**, 33–38 (1996).
98. Shen, H.-H., Thomas, R. K., Penfold, J. & Fragneto, G. Destruction and solubilization of supported phospholipid bilayers on silica by the biosurfactant surfactin. *Langmuir* **26**, 7334–7342 (2010).
99. Rondelli, V. et al. Building a biomimetic membrane for neutron reflectivity investigation: complexity, asymmetry and contrast. *Biophys. Chem.* **229**, 135–141 (2017).
100. Mattauch, S. et al. The high-intensity reflectometer of the Jülich Centre for Neutron Science: MARIA. *J. Appl. Crystallogr.* **51**, 646–654 (2018).
101. Koutsioubas, A. Combined coarse-grained molecular dynamics and neutron reflectivity characterization of supported lipid membranes. *J. Phys. Chem. B* **120**, 11474–11483 (2016).
102. Penfold, J. & Thomas, R. K. The application of the specular reflection of neutrons to the study of surfaces and interfaces. *J. Phys. Condens. Matter* **2**, 1369 (1990).
103. Rondelli, V. et al. Amyloidβ peptides in interaction with raft-mime model membranes: a neutron reflectivity insight. *Sci. Rep.* **6**, 20997 (2016).
104. Nelson, A. Co-refinement of multiple-contrast neutron/X-ray reflectivity data using MOTOFIT. *J. Appl.Crystallogr.* **39**, 273–276 (2006).
105. Boesecke, P. Reduction of two-dimensional small- and wide-angle X-ray scattering data. *J. Appl.Crystallogr.* **40**, s423–s427 (2007).
106. Lorent, J. H. et al. Plasma membranes are asymmetric in lipid unsaturation, packing and protein shape. *Nat. Chem. Biol.* **16**, 644–652 (2020).
107. R Core Team. R: a language and environment for statistical computing. *R Foundation for Statistical Computing* https://www.R-project.org/ (2020).
108. GraphPad Software. *GraphPad* www.graphpad.com (accessed 10 February 2026).
109. Gilliard, G. et al. Membrane remodelling mediates lipopeptide-induced immunity in *Arabidopsis*. *Zenodo* https://doi.org/10.5281/zenodo.8358627 (2026).
110. Gilliard, G. et al. Membrane remodelling mediates lipopeptide-induced immunity in *Arabidopsis*—RNA seq data. *Zenodo* https://doi.org/10.5281/zenodo.10013102 (2023).

Acknowledgements

This work was supported by EU Interreg V France-Wallonie-Vlaanderen (grant no. 731077) (M.O. and S.D.), the Feder programme 2021–2027 (project PHENIX biocontrol Uliege-SPW) (M.O. and M.D.), Belgian Funds for Scientific Research (grant nos T.0063.19 (M.D.), T.0081.24 (M.D. and M.O.), Weave-FWO T.0227.24/G0AH724N (M.O. and B.D.C.) and 306506201.E.069.20F (G. Gilliard)), Agence Nationale pour la Recherche in France (grant nos 24-CE20-7620 (S.M.) and 11–INBS–0010 (L.F.)), Marie Skłodowska-Curie Actions (grant no. 101104279) (J.A.), Next Generation EU (grant nos P2022J2ZC2 (V.R.) and CUP G53D23007030001 (V.R. and G. Gilliard)), Deutsche Forschungsgemeinschaft (grant nos SFB1101-A09 (J.G.), TRR356-B01 (J.G.), GR4559/4-1 (G. Grossman) and 390686111 (G. Grossman)) and the Gatsby Charitable Foundation and University of Zurich (C.Z.). We thank the ROMEO regional calculation centre at the University of Reims Champagne-Ardenne (J.-M.C.). This work benefited from the use of the MARIA neutron reflectometer at the Heinz Maier-Leibnitz

(FRM II) Zentrum in Garching (DE) under EUSMI project no. E180600111 (A.K. and V.R.). This work also benefited from the use of the ID02 beamline at the European Synchrotron Radiation Facility in Grenoble (FR) for experiment nos SC-4492 (P.B. and V.R.) and LS-3423 (G. Gilliard and V.R.). M.D. and M.O. thank the F.R.S.-FNRS for their positions as senior research associate and research director, respectively. We thank I. Feussner at the University of Goettingen for providing us with *Arabidopsis* lipid mutants, A. Martinière for providing HyPer7 lines, M. Knight at Durham University for providing Col-0^{AEQ} and J. Sprakel for the supply of N^{+}-BODIPY dye. We thank A. Anckaert, A. Legras, S. Steels, C. Helmus, E. Teyssier, A. Goret and A. Mamode-Cassim for their excellent technical support. Lipid analysis was performed on the Bordeaux-Metabolome platform (www.biomemb.cnrs.fr/en/lipidomic-plateform/). We thank the Bordeaux Imaging Center, part of the National Infrastructure France-BioImaging.

Author contributions

M.D. and M.O. designed and supervised the project. J.P., G. Gilliard, M.D., S.M. and M.O. conceptualized the project and developed the methodology. J.P., G. Gilliard, C.C., J.A., J.L., M.-D.J., S. Egli, S. Egée, G.B., H.I., A.A.-A., V.R., L.v.B., A.V.D.B., W.P.L.-L., E.D., M.N.N., M.M.-G., F.B., G.R., S. Eschrig, P.V.D.S., M.Z., A.K., P.B., L.F., O.R., B.V., V.G., C.M.-B. and Y.F.D. conducted the investigation and data analysis. J.-M.C., M.G. and L.L. did the modelling. J.P., G. Gilliard, M.D. and M.O. wrote the original draft of the paper. S.D., B.D.C., G. Grossman, J.G., S.M., D.T., T.N., S.R., M.H., S.M. and C.Z. reviewed and edited the paper.

Competing interests

The authors declare no competing interests.

Additional information

Extended data is available for this paper at https://doi.org/10.1038/s41477-026-02270-3.

Supplementary information The online version contains supplementary material available at https://doi.org/10.1038/s41477-026-02270-3.

Correspondence and requests for materials should be addressed to Magali Deleu or Marc Ongena.

Peer review information *Nature Plants* thanks Gregor Anderluh and the other, anonymous, reviewer(s) for their contribution to the peer review of this work. Peer reviewer reports are available.

Reprints and permissions information is available at www.nature.com/reprints.

Publisher's note Springer Nature remains neutral with regard to jurisdictional claims in published maps and institutional affiliations.

[1]Laboratory of Molecular Biophysics at Interfaces, TERRA Research Centre, Gembloux Agro-Bio Tech, University of Liège, Gembloux, Belgium. [2]Department of Biology, Faculty of Science and Medicine, University of Fribourg, Fribourg, Switzerland. [3]Microbial Processes and Interactions laboratory, TERRA Research Centre, Gembloux Agro-Bio Tech, University of Liège, Gembloux, Belgium. [4]MAgICS, MEDyC, CNRS UMR 7369 UFR Sciences Exactes et Naturelles, University of Reims Champagne-Ardenne, Reims, France. [5]Laboratoire de Biogenèse Membranaire, University of Bordeaux, Villenave d'Ornon, France. [6]Cellular and Molecular Pharmacology, Translational Research from Experimental and Clinical Pharmacology to Treatment Optimization, Louvain Drug Research Institute, UCLouvain, Brussels, Belgium. [7]Plant Cell Biology, TUM School of Life Sciences, Technical University of Munich, Freising, Germany. [8]Institute of Cell and Interaction Biology, CEPLAS Cluster of Excellence on Plant Sciences, Heinrich-Heine-Universität Düsseldorf, Düsseldorf, Germany. [9]UMR8227 LBI2M Sorbonne Université-CNRS, Station Biologique de Roscoff, Roscoff, France. [10]Division of Plant Biotechnics, Department of Biosystems, KU Leuven and KU Leuven Plant Institute, Heverlee, Belgium. [11]Institute of Biomolecular Science and Technology, Catholic University of Louvain, Louvain-la-Neuve, Belgium. [12]Laboratory of Chemistry of Natural Molecules, Gembloux Agro-Bio Tech, University of Liège, Gembloux, Belgium. [13]CELL Unit, De Duve Institute, UCLouvain, Brussels, Belgium. [14]School of Life Sciences Weihenstephan, Technical University of Munich, Freising, Germany. [15]Laboratory of Phytopathology, Faculty of Bioscience Engineering, Ghent University, Ghent, Belgium. [16]Department of Plant and Microbial Biology, Zurich-Basel Plant Science Center, University of Zurich, Zurich, Switzerland. [17]Sainsbury Laboratory, University of East Anglia, Norwich, UK. [18]Jülich Centre for Neutron Science at Heinz Maier-Leibnitz Zentrum, Forschungszentrum Jülich GmbH, Garching, Germany. [19]Department of Medical Biotechnology and Translational Medicine, Università degli Studi di Milano, Segrate, Italy. [20]RIBP, UMR INRAE 1488, EXEBIO Institute, University of Reims Champagne-Ardenne, Reims, France. [21]Centre of Plant Molecular Biology, Eberhard-Karls-University Tübingen, Tübingen, Germany. [22]Present address: Unité de Génie Enzymatique et Cellulaire, University of Picardie Jules Verne, Amiens, France. [23]Present address: University Bordeaux, CNRS, Bordeaux INP, CBMN, Pessac, France. [24]Present address: Institute of Bio- and Geosciences IBG-2, Forschungszentrum Jülich, Jülich, Germany. [25]Present address: Eppendorf Application Technologies, Namur, Belgium. [26]Present address: Astel Medica, Soheit-Tinlot, Belgium. [27]Present address: Bio-Life, Isnes, Belgium. [28]These authors contributed equally: Guillaume Gilliard, Jelena Pršić. [29]These authors jointly supervised this work: Magali Deleu, Marc Ongena. ✉e-mail: magali.deleu@uliege.be; marc.ongena@uliege.be

https://doi.org/10.1038/s41477-026-02270-3

Extended Data Table 1 | Neutron reflectivity parameters

a

	PLPC-Sito-GluCer bilayer			PLPC-Sito-GluCer bilayer + Srf		
	Thickness (±1Å)	**SLD (±0.05*10^{-6}Å^{-2})**	**Solvent penetration (±5%vol)**	**Thickness (±1Å)**	**SLD (±0.05*10^{-6}Å^{-2})**	**Solvent penetration (±5%vol)**
Heads in	6	1.93	25	6	1.93	25
Chains in	14	−0.28	10	14	−0.28	10
Chains out	14	−0.41	10	10	−0.38	20
Heads out	6	1.98	25	6	2	30

b

	PLPC-Sito bilayer			PLPC-Sito bilayer + Srf		
	Thickness (±1Å)	**SLD (±0.05*10^{-6}Å^{-2})**	**Solvent penetration (±5%vol)**	**Thickness (±1Å)**	**SLD (±0.05*10^{-6}Å^{-2})**	**Solvent penetration (±5%vol)**
Heads in	8	1.93	15	7	1.93	15
Chains in	14	−0.34	3	14	−0.34	3
Chains out	15	−0.34	3	13	−0.32	7
Heads out	6	1.93	15	7	1.83	25

Structural parameters used to fit the Neutron reflectivity spectra relative to the **(a)** PLPC-Sito-GluCer bilayer and **(b)** PLPC-Sito bilayer before (left) and after (right) Srf addition. The data collected from the membranes in H_2O and D_2O have been fitted together. SLD: Scattering length density.

https://doi.org/10.1038/s41477-026-02270-3

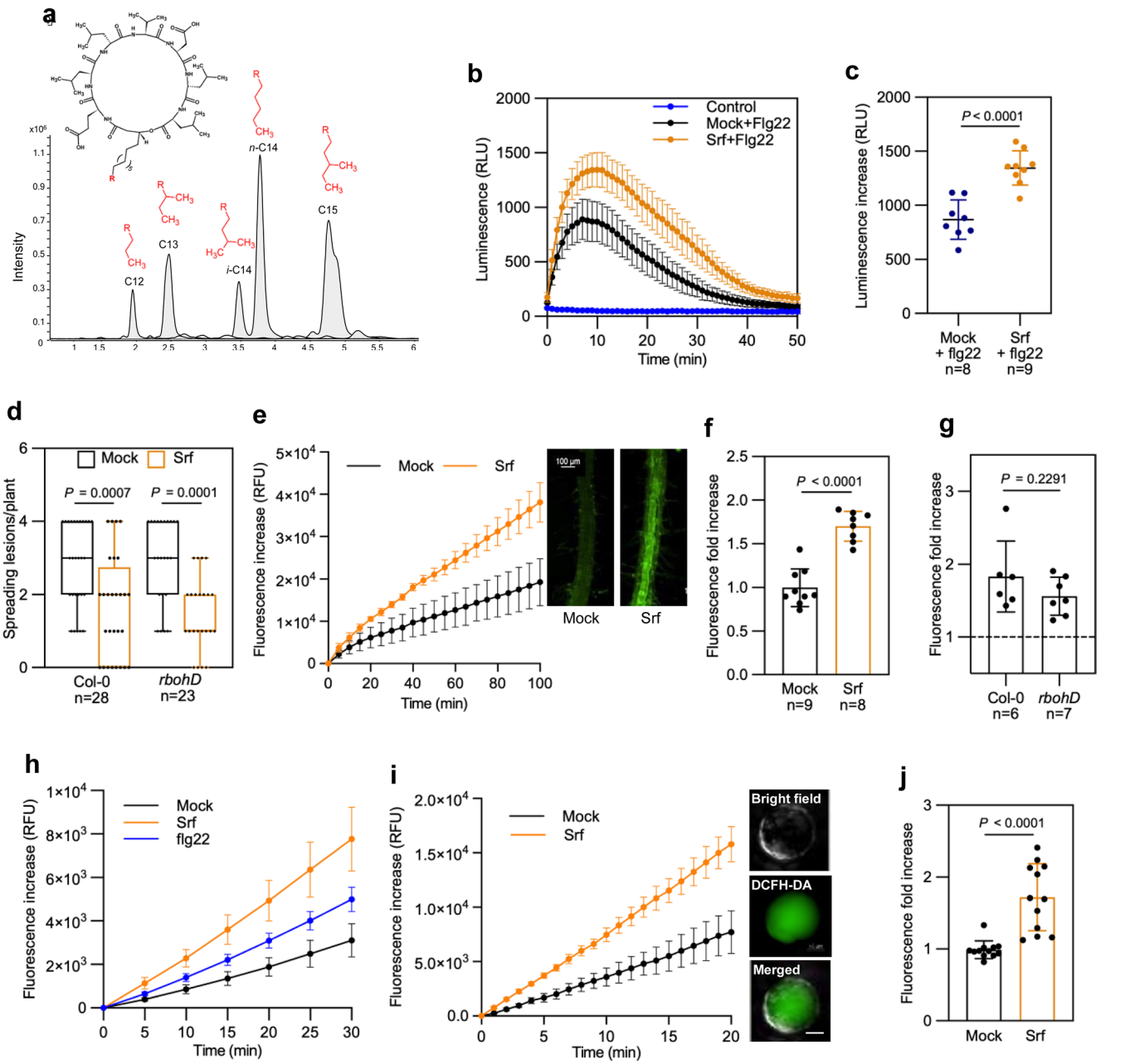

Extended Data Fig. 1 | Surfactin activates a singular ROS response in *Arabidopsis* roots associated with systemic immune activation. a, *Bacillus velezensis* produces Srf as a mixture of structural variants differing in fatty acid chain length and branching (R group in structure shown), as illustrated by UPLC-MS profiling. This diversity arises from the broad substrate selectivity of the first C-domain in the Srf NRPS enzyme, which incorporates various intracellular fatty acids into the peptide backbone. **b, c**, Systemic immune activation (SIA) using flg22 (1 µM) as MAMP. **b**, Typical trend for time-course measurement of flg22-induced $[ROS]_{apo}$ burst in leaf discs prepared from Col-0 plants pre-treated on roots with Srf 10 µM or mock (DMSO 0.1%). Control represents leaf response to water treatment. Data are from one representative experiment (Mean ± s.d., $n = 12–14$ leaf discs), **c**, Quantification of $[ROS]_{apo}$ burst ($L_{max,15\,min}$-L_0) recorded in n independent experiments as indicated. Each data point is the mean value of 3 to 8 leaf discs obtained in one single experiment. Mean ± s.d., *P*-value from two-tailed *t*-test. **d**, *B. cinerea* disease incidence in Col-0 and *rbohD* plants pre-treated at the root level with Srf (10 µM) or mock (EtOH 0.1%). Data are from three independent experiments with a total number of individual plants (n) as indicated. Box plots show median and quartiles; whiskers show range. *P*-values from two-way ANOVA with Sidak's post-test. **e, f**, Srf -induced $[ROS]_{intra}$ burst in Col-0 roots loaded with the DCFH-DA probe. **e**, Typical trend and representative images for time course of $[ROS]_{intra}$ accumulation (relative fluorescence unit, RFU) in roots after Srf treatment (10 µM) compared to mock (DMSO 0.1%). Mean ± s.d., $n = 3$ roots. **f**, $[ROS]_{intra}$ measured by fold increase in DCFH-DA fluorescence at 30 min after the addition of 10 µM Srf compared to mock-treated roots (DMSO 0.1%). Mean ± s.d., data from three independent experiments with total number of individual roots (n) as indicated; *P*-value from two-tailed *t*-test. **g**, $[ROS]_{intra}$ accumulation in Col-0 and *rbohD* roots measured by fold increase in DCFH-DA fluorescence at 30 min after Srf treatment (10 µM), relative to mock (water treatment). Mean ± s.d., data from two independent experiments. *P*-value from two-tailed *t*-test. **h**, Kinetics of $[ROS]_{intra}$ increases measured by DCFH-DA fluorescence in Col-0 roots treated with Srf (10 µM), flg22 (1 µM), or mock (water). Typical trend observed in one representative experiment with $n = 4$. **i, j**, Srf (10 µM)-induced $[ROS]_{intra}$ burst in protoplasts prepared from Col-0 roots, measured by DCFH-DA fluorescence and compared to mock (DMSO 0.1%). **i**, Time course $[ROS]_{intra}$ production typically observed following Srf or mock treatment. Mean ± s.d., $n = 4$; representative of four experiments. Right, images of Srf-responsive protoplast loaded with DCFH-DA (Bar = 5 µm). **j**, Fold increase in $[ROS]_{intra}$ at 5 min post-Srf treatment in Col-0 protoplasts vs. mock. Mean ± s.d., $n = 12$, data grouped from four experiments; *P*-value from two-tailed *t*-test.

https://doi.org/10.1038/s41477-026-02270-3

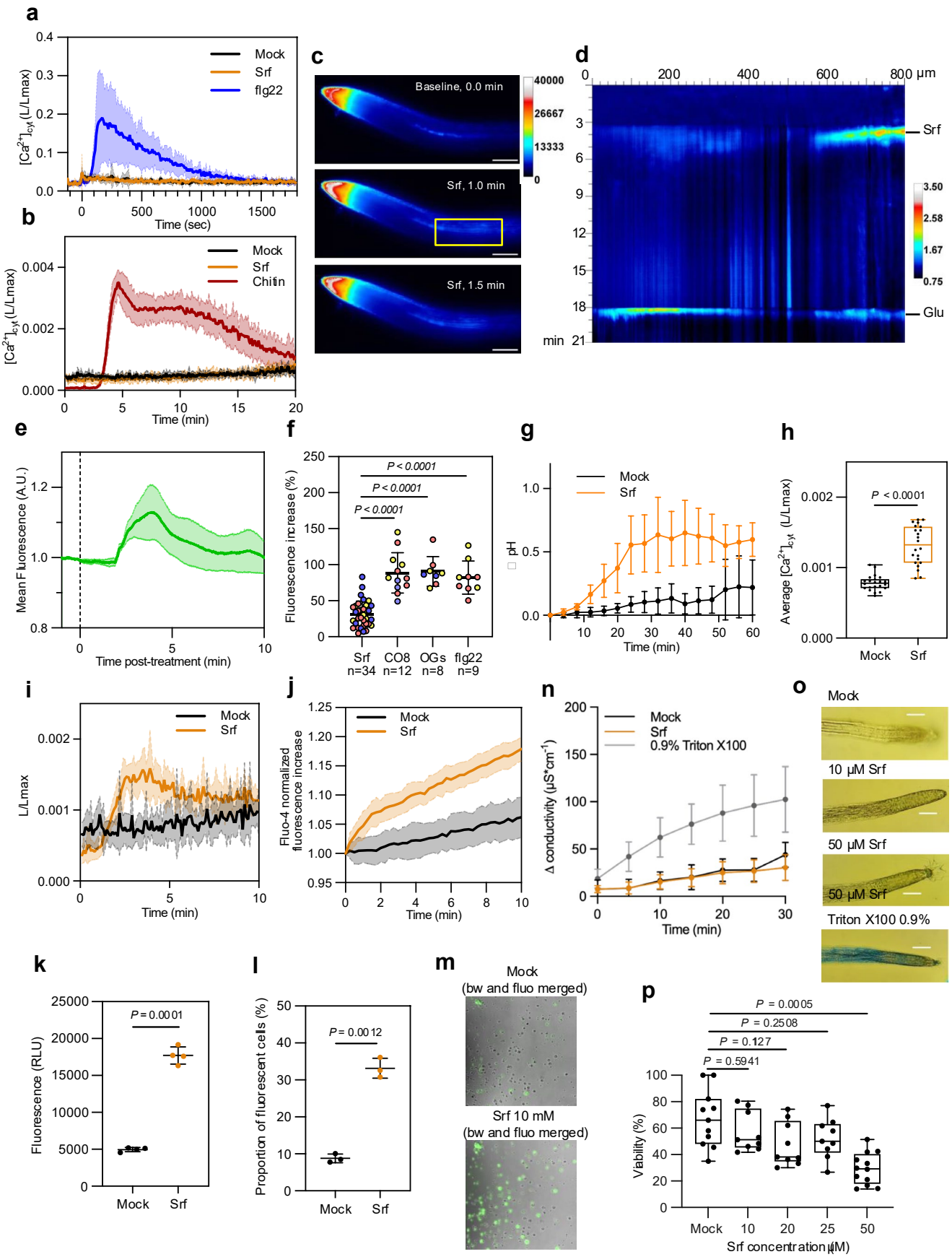

Extended Data Fig. 2 | See next page for caption.

https://doi.org/10.1038/s41477-026-02270-3

Extended Data Fig. 2 | Ion fluxes triggered by Srf in root cells. a, $[Ca^{2+}]_{cyt}$ kinetics in Col-0^{AEQ} roots treated with Srf (10 µM), flg22 (1 µM) or mock (EtOH 0.1%). Results are represented as luminescence counts per second relative to total luminescence counts remaining (L/L_{max}; mean ± s.d., $n = 6$). Three independent experiments yielded similar results. **b**, $[Ca^{2+}]_{cyt}$ kinetics in Col-0^{AEQ} roots upon treatment with Srf (10 µM), chitin (100 µg/mL) or mock (EtOH 0.1%). L/L_{max} mean values ± s.d. ($n = 8$; two independent experiments). **c**, Time-lapse images of root tip and elongation zone following Srf treatment (10 µM). Yellow boxes highlight responsive zones. **d**, Kymograph displaying the Ca^{2+} sensor R-GECO1 signal normalized to the average baseline intensity of the first 3 minutes. Treatment with Srf was performed 3 minutes after baseline imaging. Positive control (L-Glutamic acid, 1 mM, denoted Glu) was administered after 18 minutes. **e**, R-GECO signal for $[Ca^{2+}]_{cyt}$ (mean fluorescence intensity, $n = 4$ roots) in the root tip of roots following treatment with flg22 (1 µM); timing of treatment marked by vertical dashed line. **f**, Quantification of $[Ca^{2+}]_{cyt}$ responses in UBQ10::GCaMP3 line after Srf (10 µM) or MAMP treatments (CO8, 150 µg/mL; OGs (oligogalacturonides DP_{10-15}), 100 µg/mL; flg22 1 µM). Fluorescence increase ($(F_{max}-F_0)/F_0$) in the ROI; Mean ± s.d. calculated from grouped data collected in four independent experiments for Srf and in three assays for MAMPs. **g**, pH variation in Col-0 root medium after addition of Srf (10 µM) or mock (EtOH 0.1%). Values normalized to time 0. One representative experiment ($n = 4$) from two experiments showing similar results. **h**, $[Ca^{2+}]_{cyt}$ in Col-0^{AEQ} protoplasts after Srf (10 µM) or mock (protoplast buffer) treatment. Box plots show medians, quartiles, and ranges. ($n = 22$, data grouped from four experiments); Results are represented as luminescence counts per second relative to total luminescence counts remaining (L/L_{max}). **i**, $[Ca^{2+}]_{cyt}$ kinetics in Col-0^{AEQ} protoplasts after Srf (10 µM) or mock (protoplast buffer) treatment. Mean ± s.d., $n = 12$. **j**, Increase in $[Ca^{2+}]_{cyt}$ measured with Fluo-4 in protoplasts ($n = 14$) following Srf (10 µM) or mock (WI_{Ca}) treatment. **k**, PM depolarization in Col-0 protoplasts stained with DIBAC(4)3 following treatment with Srf (10 µM) or mock (DMSO 0.1%). Data grouped from four independent experiments ($n = 4$) and each data point is the mean of 4 wells in one independent experiment. **l, m**, Proportion of fluorescent protoplasts following treatment with Srf (10 µM) or mock (DMSO 0.1%) and staining with DIBAC4(3) probe (representative microscopic images in **m**). Data grouped from three independent experiments ($n = 3$) and each data point is the mean of 4 wells in one independent experiment. Mean ± s.d.
n, Conductivity variation in Col-0 root medium after treatment with Srf (10 µM), mock (EtOH 0.1%), or Triton X-100 (0.9%). Mean ± s.d. ($n = 10$; two experiments). **o**, Cell viability in roots treated with Srf (10 or 50 µM), EtOH 0.5% (mock - negative control), or Triton X-100 (0.9%, positive control), visualized by Evans blue. Experiments were performed on three different individuals for each treatment with similar results. **p**, Protoplast viability with increasing Srf concentrations or mock (EtOH 0.5%), assessed with fluorescein diacetate. Mean ± s.d., $n = 9$, 11 or 12, data from three experiments). In **f** and **p**, *P*-values are from one-way ANOVA with Dunnett's T3 post-test. In **h**, **k**, **l**, **m**, *P*-values from two-tailed Welch's t-test.

https://doi.org/10.1038/s41477-026-02270-3

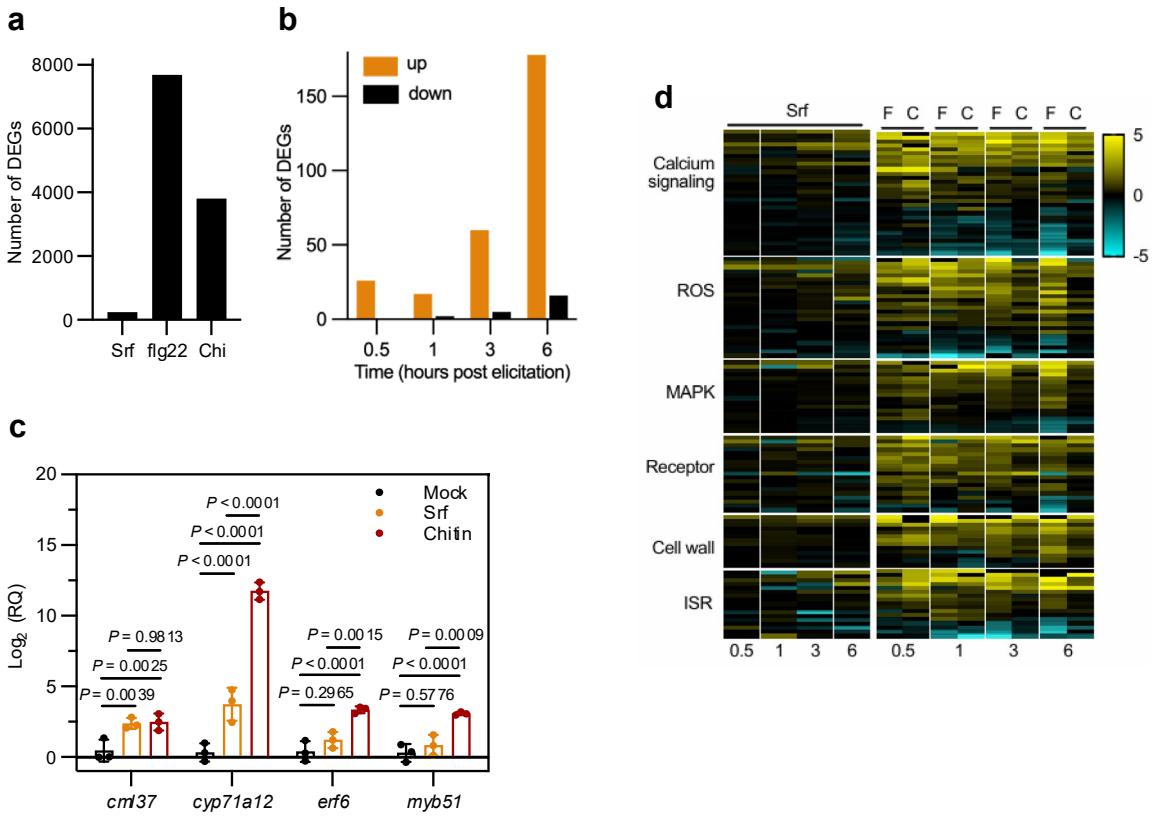

Extended Data Fig. 3 | Surfactin induces a limited transcriptional change. **a**, Comparison of the total Srf (10 µM)-induced DEGs (Log2 Fold Change > 1, $p < 0.05$) in *Arabidopsis* root cells (RNA-seq) with those reported in response to flg22 (1 µM) and chitin (Chi, 1 mg/mL)[30]. **b**, Number of DEGs over all time points (30 min, 1 h, 3 h and 6 h post-treatment) in Srf (10 µM)-treated roots. **c**, RT-qPCR on some genes that were found differentially expressed (up- or down-regulated) in RNAseq and selected for their involvement in signalling cascade and/or global immune response. *CML37*, Ca^{2+}-binding calmodulin sensor; *ERF6*, transcription factor involved in hormonal crosstalk, *MYB51*, control of indole glucosinolate biosynthesis and callose deposition; *CYP71A12*, synthesis of camalexin. Treatment with chitin was included to confirm the trends in differential expression reported for those genes in RNAseq data from[30]. Data show relative expression (normalized to the housekeeping gene *UBQ5)* in Col-0 roots 6 h after treatment with Srf (10 µM) or chitin (100 µg/mL), Means ± s.d. from one representative experiment ($n = 3$ biological replicates, extracts prepared from eight roots each). The experiment was repeated twice with similar results. *P*-values from two-way ANOVA with Tukey's post-test. **d**, Heatmap of immune-related gene expression modulated by Srf (10 µM) compared with flg22 (F, 1 µM) and chitin (C, 1 mg/mL), based on published data[30]. This includes genes encoding receptor-like kinases, or genes associated with ROS production, Ca^{2+} signaling, MAPK cascades, pathogenesis-related (PR) proteins, callose deposition or lignification. Colour scale indicates Log2 Fold Change.

https://doi.org/10.1038/s41477-026-02270-3

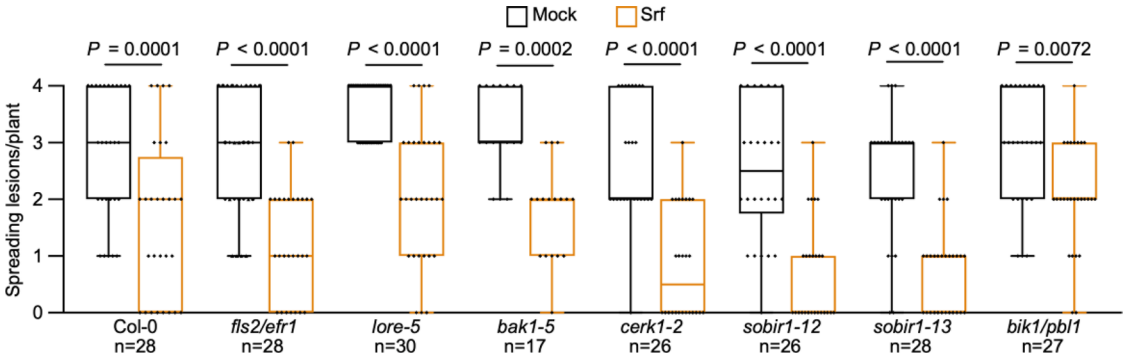

Extended Data Fig. 4 | Surfactin perception is not mediated by typical PRR systems. Disease incidence upon leaf infection by *B. cinerea* in plants pretreated with Srf (10 µM) or mock (EtOH 0.1%) at the root level in *Arabidopsis* wild-type plants (Col-0) or mutants lacking functional receptors required for the detection of either bacterial proteinaceous immunogenic patterns (*fls2/efr*[66]) or acyl chain epitopes (*lore*-5[72]), co-receptors (*bak1*-5[68], *cerk1*-2[69], *sobir1*-12 and *sobir1*-13[70]), or receptor-like cytoplasmic kinase (*bik1/pbl1*[67]). Box plots show medians, quartiles, and ranges. *P*-values from two-way ANOVA with Sidak's multiple comparison. Data pooled from three independent experiments, *n* individuals are shown below each genotype).

https://doi.org/10.1038/s41477-026-02270-3

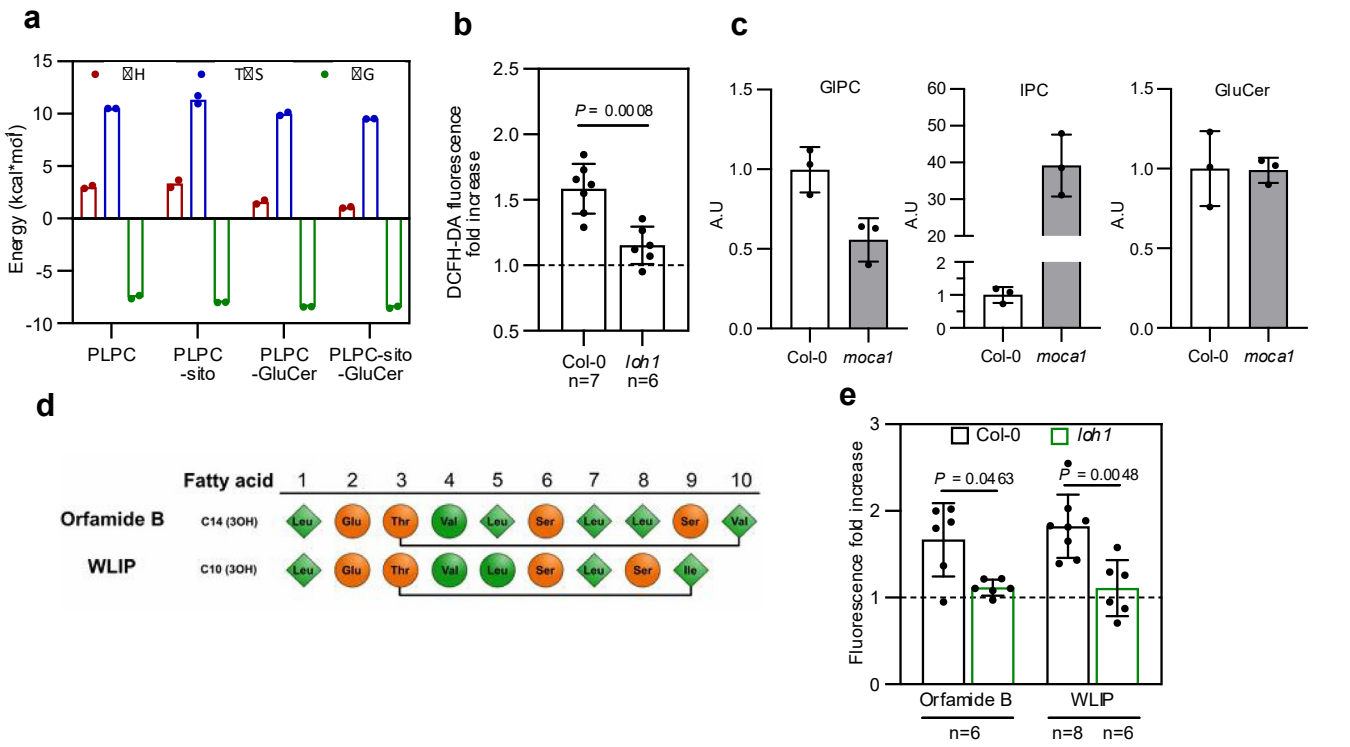

Extended Data Fig. 5 | GluCer Sphingolipids are key components for CLP-membrane interaction and CLP-mediated immune activation. **a**, Thermodynamic parameters associated with the different ITC experiments: variation of enthalpy (ΔH), variation of entropy (T*ΔS) and variation of Gibbs free energy (ΔG). Data show mean from two independent replicates. **b**, $[ROS]_{intra}$ accumulation in roots of Col-0 and its *loh1* mutant measured by DCFH-DA fluorescence fold increase 30 min after Srf (10 µM) vs mock (water) treatment. Mean ± s.d., total number of roots (*n*) indicated are from two independent experiments). *P*-value from two-tailed *t*-test. **c**, Sphingolipidomic analysis (GIPC, IPC and GluCer level) of *Col-0* and *moca1* leaves by LC-MSMS performed according to[41]. **d**, Structures of the CLPs produced by *Pseudomonas* sp. used in this study. Rhombus indicates L- and circle D-amino acids; green, nonpolar; orange, polar. **e**, $[ROS]_{intra}$ production in roots of Col-0 and *loh1* mutant measured by DFCH-DA fluorescence fold increase vs mock (water), 30 min after treatment with orfamide B (10 µM) or WLIP (10 µM). Mean ± s.d., *n* individuals from two experiments. *P*-values from Brown-Forsythe and Welch's ANOVA with Tamhane's T2 post-test.

https://doi.org/10.1038/s41477-026-02270-3

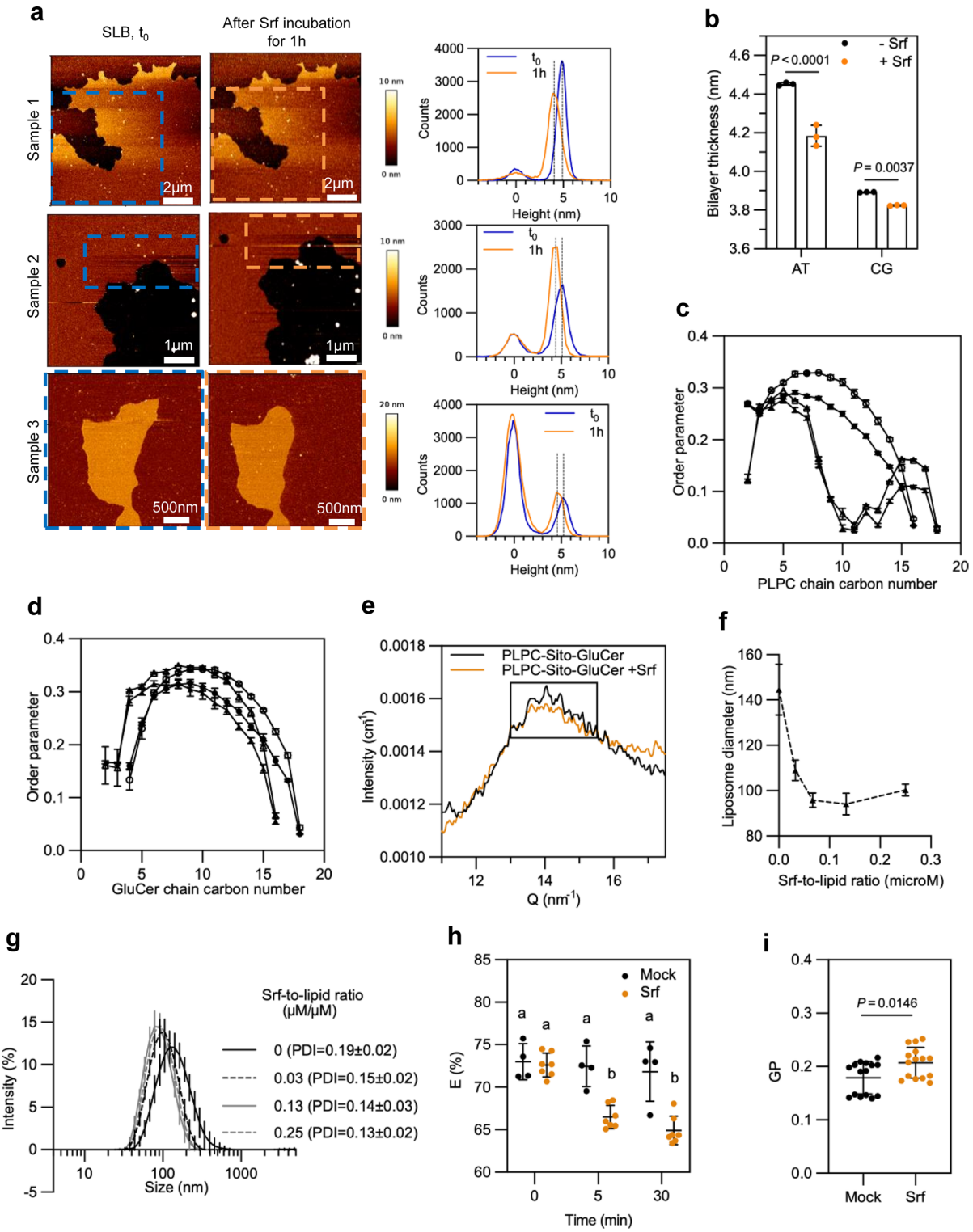

Extended Data Fig. 6 | See next page for caption.

https://doi.org/10.1038/s41477-026-02270-3

Extended Data Fig. 6 | Impact of Srf on thickness and lipid ordering of biomimetic membranes. a, Bilayer thickness by Atomic Force Microscopy (AFM). Left: AFM topographic images of PLPC-Sito-GluCer bilayers before (t_0) and after 1 h incubation with Srf (3 µM). Right: Height density profiles measured on selected areas before (blue) and after (orange) Srf treatment. Data from three independent samples. **b**, Bilayer thickness data calculated from MD simulations in the absence or presence of Srf from AT and CG simulations. Mean ± s.d. from three simulations. Thickness corresponds to the distance between phosphate atoms of PLPC from the upper and lower leaflets within a PLPC-Sito-GluCer bilayer. *P*-value from two-way ANOVA with Sidak's post-test. **c,d**, Order parameter (mean ± s.d., three experiments) for PLPC acyl chains (C16, C18:2) and GluCer N-acyl and sphingosine chains, calculated from AT simulations without (white) or with (black) Srf. **c**, PLPC acyl chains C16 are circles and C18:2 triangles. **d**, N-acyl chain of GluCer is circles and the sphingosine chain is triangles. **e**, Wide angle X-ray scattering (WAXS) spectra displaying **a** typical peak for lipid bilayer, interpreted as a measure of the average chain-to-chain distance. Data shows a shift to lower q-vector values in presence of Srf, indicating increased chain disorder in the bilayer. **f**, Hydrodynamic diameter (mean ± s.d., $n = 6$) of liposomes measured by Dynamic Light Scattering (DLS) at increasing Srf-to-lipid ratios. **g**, Size distribution of liposomes at various Srf-to-lipid ratios obtained by weighting the DLS data by intensity. Data from at least two independent liposome batches. **h**, FRET Efficiency (E, %) between Fluorescein DHPE (donor) and 18:1 Liss Rhodamine PE (acceptor) for PLPC-Sito-GluCer LUVs with Srf (10 µM) or mock (DMSO 0.1%) at three different time courses. $n = 4$ (mock) or 6 (Srf) replicates from two independent experiments. Letters represent statistically different groups at $P < 0.05$ (Brown-Forsythe and Welch's ANOVA and Tamhane's T2 multiple comparisons test). **i**, Global membrane stiffening measured by Laurdan generalized polarization (GP) for PLPC-Sito-GluCer liposomes with Srf (10 µM) or mock (EtOH 0.1%). Mean ± s.d. ($n = 15$; five experiments). *P*-value from two-tailed t-test.

https://doi.org/10.1038/s41477-026-02270-3

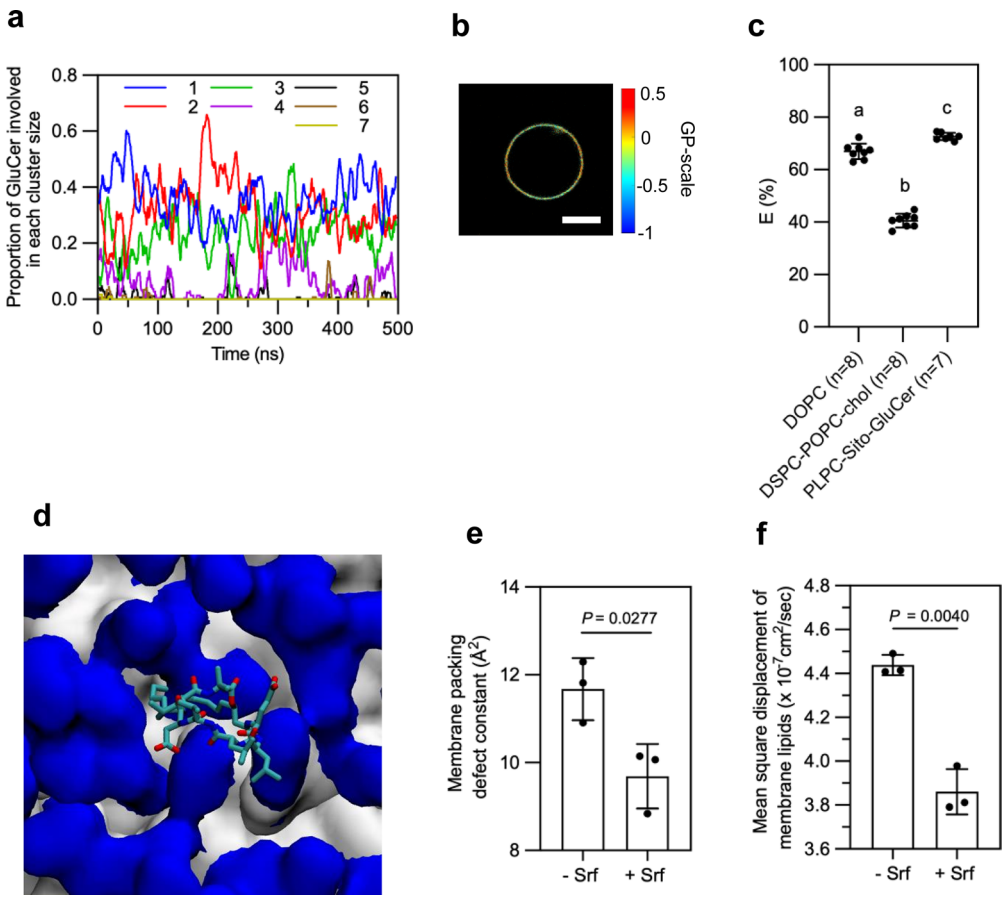

Extended Data Fig. 7 | Nanoscale modifications in lipid organization induced by Srf. a, Proportion of GluCer involved in each GluCer cluster size (1–7 molecules) from AT simulations. Representative data of one experiment out of three with similar results (see Supplementary Fig. 4 for replicates). **b**, GP imaging of C-Laurdan in PLPC-Sito-GluCer GUVs. Higher GP observed in the horizontal plane is an artefact due to photoselection effect of Laurdan molecules that are aligned in parallel to the polarization angle of the LASER. Scale bar: 5 µm. **c**, FRET efficiency (%) between Fluorescein-DHPE (donor) and Liss Rhodamine-PE (acceptor) in DOPC (liquid-disordered), DSPC-POPC-Chol (40/40/20 %mol) (nanoscopic phase separation), and PLPC-Sito-GluCer (60/20/20 %mol) membranes. Plant model shows no evidence of nanodomains. Data from two experiments are grouped and total *n* are indicated. Letters represent statistically different groups ($P < 0.05$, Brown-Forsythe and Welch's ANOVA with Tamhane's T2). **d**, Top view of PLPC-Sito-GluCer bilayer after 2879 ns of AT simulation, showing Srf (cyan sticks) insertion involving its acyl chain among membrane lipid acyl chains (white surface) and lipid polar heads (blue). **e**, Membrane packing defect constant calculated from AT simulations in PLPC-Sito-GluCer with or without Srf. **f**, Srf reduces lateral lipid mobility based on mean square displacement (MSD) of lipids in PLPC-Sito-GluCer membranes with (+ Srf) or without Srf (-Srf), from CG simulations. In **e** and **f**, data are mean ± s.d. obtained from $n = 3$ different simulations. *P*-values from two-tailed Welch's t-test.

https://doi.org/10.1038/s41477-026-02270-3

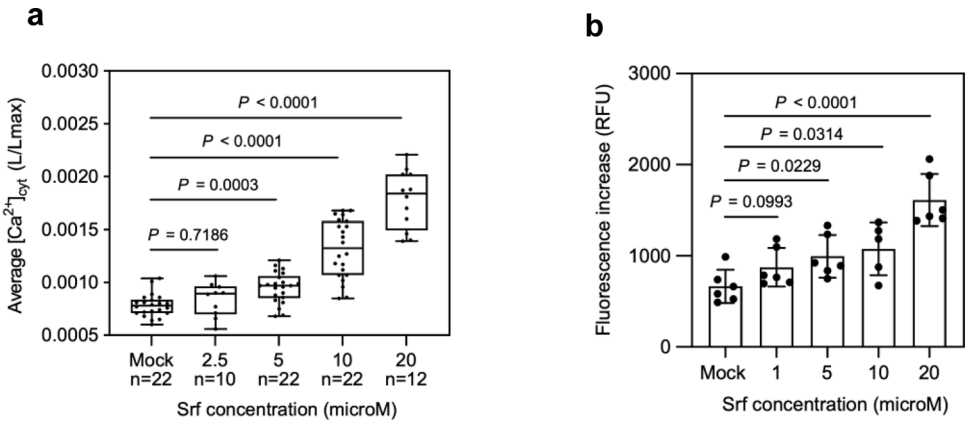

Extended Data Fig. 8 | Immune activation by Srf requires threshold micromolar concentrations. a, Dose-dependent $[Ca^{2+}]_{cyt}$ increase induced by Srf in root protoplasts of *Arabidopsis* Col-0^{AEQ} compared to mock (EtOH 0.1%). Data show the average of luminescence (L/L_{max}) between 1.5 and 4 min after Srf (10 µM) treatment (maximal values). Box plots show medians, quartiles, and ranges, data are from five independent experiments and total *n* are indicated. *P*-values from Welch and Brown-Forsythe ANOVA with Dunnett's T3 post-test. **b**, Dose-dependent $[ROS]_{intra}$ induction by Srf (10 µM) measured with DCFH-DA in root protoplasts compared to mock (EtOH 0.1%). Graph represents mean ± s.d., *n* = 6 roots from two independent experiments, *P*-values from two-tailed unpaired t-test with Welch's correction.

https://doi.org/10.1038/s41477-026-02270-3

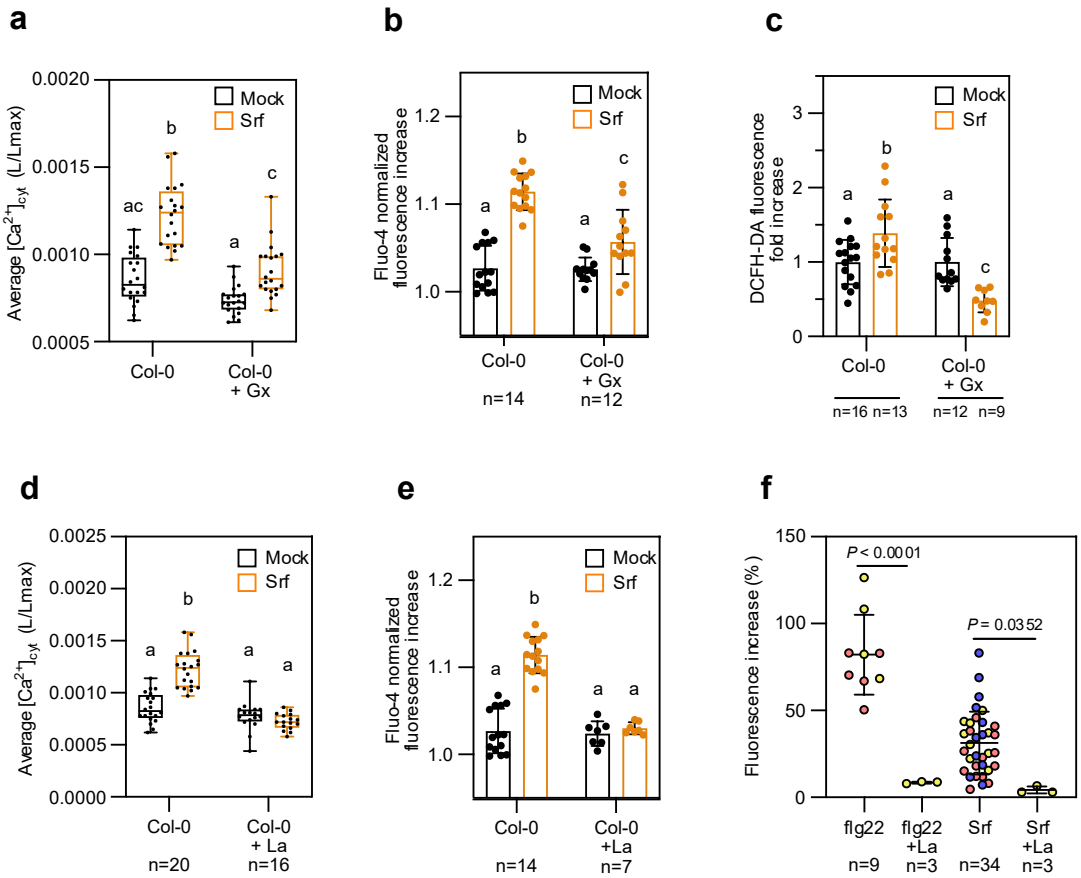

Extended Data Fig. 9 | Impact of channel blockers on calcium and ROS responses to Srf treatment. a, $[Ca^{2+}]_{cyt}$ levels in Col-0^{AEQ} protoplasts upon Srf (10 µM) or mock (WI_{Ca}), with or without pre-incubation with the mechanosensitive channel blocker GsMTX-4 (+Gx). *n* = 20 from four independent experiments. **b**, $[Ca^{2+}]_{cyt}$ response measured with the Fluo4-AM probe in Col-0 protoplasts treated with Srf (10 µM) or mock (WI_{Ca}), with or without pre-incubation with GsMTX-4 (+ Gx). Mean ± s.d., data are from four independent experiments with total *n* indicated. **c**, $[ROS]_{intra}$ accumulation in Col-0 roots 30 min after Srf (10 µM) or mock (water) treatment, in presence or absence of GsMTX-4 (+ Gx). Data are expressed as fold increase in DCFH-DA fluorescence compared to mock. Mean ± s.d., data are from three independent experiments with total *n* indicated. **d**, $[Ca^{2+}]_{cyt}$ signal in Col-0^{AEQ} protoplasts following Srf (10 µM) or mock (WI_{Ca}) treatment with or without pre-incubation with the calcium channel blocker $LaCl_3$ (+ La). Data are from four independent experiments with total *n* indicated. **e**, Calcium influx in Col-0 protoplasts measured via Fluo4-AM fluorescence after Srf (10 µM) or mock (WI_{Ca}) treatment, with or without $LaCl_3$ pre-treatment. Data are normalized fluorescence increases. Mean ± s.d., data are from at least two independent experiments with total *n* indicated. **f**, $[Ca^{2+}]_{cyt}$ signal in UBQ10::GCaMP3 roots treated with Srf (10 µM) or flg22 (1 µM) as MAMP, with (+ La) or without $LaCl_3$ pre-treatment. Signal quantified as fluorescence increase. Mean ± s.d., total *n* indicated. *P*-values from unpaired two-tailed t-test with Welch's correction. In **a** and **d**, data show the average of luminescence (L/L_{max}) between 1.5 and 4 min post-treatment with Srf. Box plots show medians, quartiles, and ranges. Letters represent statistically different groups ($P < 0.05$, two-way ANOVA with Bonferroni's post-test). In **b**, **c** and **e**, letters indicate statistically different groups at $P < 0.05$, two-way ANOVA with Tukey's post-test.

nature portfolio

Corresponding author(s): Marc Ongena

Last updated by author(s): 15/11/2025

Reporting Summary

Nature Portfolio wishes to improve the reproducibility of the work that we publish. This form provides structure for consistency and transparency in reporting. For further information on Nature Portfolio policies, see our Editorial Policies and the Editorial Policy Checklist.

Statistics

For all statistical analyses, confirm that the following items are present in the figure legend, table legend, main text, or Methods section.

n/a	Confirmed	
☐	☒	The exact sample size (*n*) for each experimental group/condition, given as a discrete number and unit of measurement
☐	☒	A statement on whether measurements were taken from distinct samples or whether the same sample was measured repeatedly
☐	☒	The statistical test(s) used AND whether they are one- or two-sided *Only common tests should be described solely by name; describe more complex techniques in the Methods section.*
☐	☒	A description of all covariates tested
☐	☒	A description of any assumptions or corrections, such as tests of normality and adjustment for multiple comparisons
☐	☒	A full description of the statistical parameters including central tendency (e.g. means) or other basic estimates (e.g. regression coefficient) AND variation (e.g. standard deviation) or associated estimates of uncertainty (e.g. confidence intervals)
☐	☒	For null hypothesis testing, the test statistic (e.g. *F*, *t*, *r*) with confidence intervals, effect sizes, degrees of freedom and *P* value noted *Give P values as exact values whenever suitable.*
☒	☐	For Bayesian analysis, information on the choice of priors and Markov chain Monte Carlo settings
☒	☐	For hierarchical and complex designs, identification of the appropriate level for tests and full reporting of outcomes
☒	☐	Estimates of effect sizes (e.g. Cohen's *d*, Pearson's *r*), indicating how they were calculated

Our web collection on statistics for biologists contains articles on many of the points above.

Software and code

Policy information about availability of computer code

Data collection	All experimental data were collected with softwares associated to the specific equipment. No specific code was created. Fluorescence/luminescence: Spark® microplate reader (Tecan) FLIM: high-resolution, inverted, OpenFrame-based epifluorescence microscopy (Cairn GmbH) Calcium signal: Nikon SMZ1270 stereomicroscope : NIS-elements AR 5_30_05 Calcium signal: LSM980 microscope (Zeiss, Germany) GP imaging: inverted Leica SP8 microscope with FLIM acquisition and integration done with PiqoQuant Symphotime DLS: Zetasizer Nano DLS instrument (Malvern Panalytical) AFM: quantitative imaging (QI) mode of a JPK Nanowizard III setup LC-MSMS for camalexin: Agilent 1290 Infinity II coupled with Jet Stream ESI-Q-TOF 6530 ITC: VP-ITC Microcalorimeter (Microcal, Northampton, USA) RT-qPCR: ABI step-one qPCR instrument (Applied Biosystems) with software version 2.3. Paired-end reads trimmed with fastp, aligned using STAR, transcript abundances quantified with Salmon. Membrane depolarization: inverted Zeiss LSM880. Electrophysiology: patch-clamp amplifier (RK400, Biologic, Claix, France) and micro1401 digitizer (CED, Cambridge, UK). Intracellular ROS using the biosensor HyPer7-cyto: ZEISS LSM 880 confocal laser scanning microscope. LC-MS/MS for lipidomics performed on a QTRAP 6500 (ABSciex) mass spectrometer coupled to a 1290 Infinity II LC system (Agilent)
Data analysis	All statistical analyses were performed in GraphPad Prism 8.0.1. Calcium signal RGECO epifluorescence microscopy: FIJI Image J (https://doi.org/10.1002/0471142727.mb1420s92) Calcium influx UBQ10::GCaMP3 NIS-elements AR 5_30_05

FLIM images:SymPhoTime64 software (PicoQuant, Germany)
GP images: home-written Matlab® routine available in: Nat Chem Biol 16, 644–652 (2020).
SAXS data: SAXS utilities analysis package [http://www.sztucki.de/SAXSutilities/]
NR data: MotoFit program available in: J Appl Cryst 39, 273–276 (2006)
ITC data analyzed with software Origin v7 (Originlab, Northampton, USA)
LC-MSMS camalexin: Masshunter (Agilent)
RT-qPCR: differential expression analysis with PyDESeq2.
Electrophysiology: WinEDR software (v4.1.6, J. Dempster, Strathclyde University, UK)
Membrane depolarization: Fiji as available in Nat Methods 9, 676–682 (2012)
Aequorin: FlagScreen R-script available in: Molecular Plant 5, 115–130 (2012)
ROS for Hyper7-cyto: FIJI.
Lipidomics: MultiQuant software version 3.0 (ABSciex)
Molecular Dynamics: GROMACS v2020.4 (SoftwareX 1–2, 19–25 (2015)), MDAnalysis (J Comput Chem 32, 2319–2327(2011)), Lipyphilic (J. Chem. Theory Comput. 17, 5907–5919 (2021)), PackMEM (Biophys J 115, 436–444 (2018)), LipidDyn (Computational and Structural Biotechnology Journal 20, 3604–3614 (2022)), PYMOL v1.8 and VMD (Journal of Molecular Graphics 14, 33–38 (1996)).

For manuscripts utilizing custom algorithms or software that are central to the research but not yet described in published literature, software must be made available to editors and reviewers. We strongly encourage code deposition in a community repository (e.g. GitHub). See the Nature Portfolio guidelines for submitting code & software for further information.

Data

Policy information about availability of data

All manuscripts must include a data availability statement. This statement should provide the following information, where applicable:

- Accession codes, unique identifiers, or web links for publicly available datasets
- A description of any restrictions on data availability
- For clinical datasets or third party data, please ensure that the statement adheres to our policy

All essential data in direct support to the conclusions are provided in the submitted material as main figs, extended data figs or table or as supplementary information. All raw/original data used in graphs and materials related to all experiments except RNAseq are available at DOI: 10.5281/zenodo.8358628. RNAseq data are available at DOI: 10.5281/zenodo.10013102.

Research involving human participants, their data, or biological material

Policy information about studies with human participants or human data. See also policy information about sex, gender (identity/presentation), and sexual orientation and race, ethnicity and racism.

Reporting on sex and gender	N/A
Reporting on race, ethnicity, or other socially relevant groupings	N/A
Population characteristics	N/A
Recruitment	N/A
Ethics oversight	N/A

Note that full information on the approval of the study protocol must also be provided in the manuscript.

Field-specific reporting

Please select the one below that is the best fit for your research. If you are not sure, read the appropriate sections before making your selection.

☒ Life sciences ☐ Behavioural & social sciences ☐ Ecological, evolutionary & environmental sciences

For a reference copy of the document with all sections, see nature.com/documents/nr-reporting-summary-flat.pdf

Life sciences study design

All studies must disclose on these points even when the disclosure is negative.

Sample size	Sample size in every experiment was determined based on a combination of factors, including standard practices in plant biology research, in experimental/in silico biophysics but also according to the objectives of the experiments. In all instances, we consider that sample sizes were adapted to reach statistical relevance and are therefore sufficient to support the conclusions of this study.
Data exclusions	No data were excluded.
Replication	As for sample sizes, the number of independent experiments for each type of assay/experiment has been adapted according to the type,

Replication	objective and inherent variability to meet robustness of the observations after statistical treatment. For some biophysics such as NR, SAXS and AFM, there is de facto few space for performing a large number of independent experiments but there is much less inherent variability compared with biological/biochemical assays involving real plants. We thus believe in the robustness of all kind of data generated.
Randomization	Methodologies related to plant experiments were conceived in a randomized design in order to minimize selection bias and consequences of uncontrolled variables.
Blinding	No specific blinding was applied but data analysis/quality check/relevance was performed independently by at least two different persons in most experiments. Of course, we implemented consistent experimental protocols and standardized data analysis pipelines for all samples, contributing to minimize bias.

Reporting for specific materials, systems and methods

We require information from authors about some types of materials, experimental systems and methods used in many studies. Here, indicate whether each material, system or method listed is relevant to your study. If you are not sure if a list item applies to your research, read the appropriate section before selecting a response.

Materials & experimental systems

n/a	Involved in the study
☒	☐ Antibodies
☒	☐ Eukaryotic cell lines
☒	☐ Palaeontology and archaeology
☒	☐ Animals and other organisms
☒	☐ Clinical data
☒	☐ Dual use research of concern
☐	☒ Plants

Methods

n/a	Involved in the study
☒	☐ ChIP-seq
☒	☐ Flow cytometry
☒	☐ MRI-based neuroimaging

Dual use research of concern

Policy information about dual use research of concern

Hazards

Could the accidental, deliberate or reckless misuse of agents or technologies generated in the work, or the application of information presented in the manuscript, pose a threat to:

No	Yes
☒	☐ Public health
☒	☐ National security
☒	☐ Crops and/or livestock
☒	☐ Ecosystems
☒	☐ Any other significant area

Experiments of concern

Does the work involve any of these experiments of concern:

No	Yes
☒	☐ Demonstrate how to render a vaccine ineffective
☒	☐ Confer resistance to therapeutically useful antibiotics or antiviral agents
☒	☐ Enhance the virulence of a pathogen or render a nonpathogen virulent
☒	☐ Increase transmissibility of a pathogen
☒	☐ Alter the host range of a pathogen
☒	☐ Enable evasion of diagnostic/detection modalities
☒	☐ Enable the weaponization of a biological agent or toxin
☒	☐ Any other potentially harmful combination of experiments and agents

Plants

Seed stocks	Arabidopsis wild-type Col-0 and mutants of RKs and RLPs fls2/efr1, bak1-5, bkk1-1, bak1-5/bkk1-1, bik1/pbl1, cerk1-2, dorn1-1, pad3 and rbohd are maintained in our laboratory. sobir1-12, sobir1-13, are from F. Brunner (University of Tübingen). The lipid mutant loh1 is from I. Feussner lab (Goettingen University) and MOCA1 is maintained in the S. Mongrand lab. Reporter lines Col-0aeq and mutant lore-5 are maintained in the labs of Stefanie Ranf. R-GEC01 is at Guido Grossmann lab. The Ubq10::CaMV35mutant is from Corrie Pieterse and P. Ronald (Utrecht University). Mutants of RKs and RLPs fls2/efr1, bak1-5, bkk1-1, bak1-5/bkk1-1, bik1/pbl1, cerk1-2, dorn1-1, pad3, rbohd, msl4/5/6/9/10 and moca1/2 are from Cyril Zipfel. All mutants are in the Col-0 background.
Novel plant genotypes	To monitor intracellular reactive oxygen species (ROS) accumulation, Arabidopsis thaliana lines expressing the genetically encoded biosensor HyPer7 were used and provided by A. Martinière (University of Montpellier). The HyPer7 sensor was introgressed into mutant backgrounds (moca1, loh1, msl4/5/6/9/10, and moca1/2) through genetic crosses and floral dip transformation.
Authentication	For HyPer7 biosensors, F2 progeny were screened for homozygous mutants carrying the sensor via fluorescence phenotyping and sequencing.